Supporting Information

Controllable Construction of Ho_2O_3 Nanomaterials with Different Dimensions (1D, 2D, 3D) for Real-time Monitoring Human Breathing and Body Surface Humidity Detection

Chuanyu Guo, [a] Xin Dong, [a] Xianfa Zhang, [a] Xiaoli Cheng, [a] Qi Li, [a] Yujing Sun, [b] Wei Liu, [b] Lihua Huo, *[a] and Yingming Xu*[a]

[a] *Key Laboratory of Functional Inorganic Material Chemistry Ministry of Education, School of Chemistry and Materials Science, Heilongjiang University, Harbin, 150080, P. R. China.*

[b] *The Key Laboratory of Low-Carbon Chemistry & Energy Conservation of Guangdong Province, School of Materials Science and Engineering, Sun Yat-sen University, Guangzhou, 510275, P. R. China.*

*Corresponding author. Tel/Fax: +86 0451 86608426.
E-mail address: xuyingming@hlju.edu.cn; huolihua@hlju.edu.cn.

Part I: Experimental Section

Characterization: The thermogravimetric characterization was carried out by TG/DTA6300 thermogravimetric analyzer (TG) from Perkin Elmer, USA. The temperature range was 30-800°C, and the heating rate was 10°C·min^{-1} in air steam. The phase and purity of the produce were characterized by D/MAX-IIIB X-ray diffractometer (XRD) from Rigaku, Japan, in the range of 10-80° under Cu-Kα radiation (λ = 1.5406 Å). The infrared spectra were recorded on Nicolet iS10 Fourier transform infrared spectrometer (FT-IR) from Thermo, USA. The morphology and microstructure of the samples were characterized by S4800 scanning electron microscope (SEM) from HTIACH, Japan; JEOL-JEM-2010 transmission electron microscope (TEM) from Japan and MultiMode8 atomic force microscope (AFM) from Bruker, Germany. The specific surface area and pore size were measured at 77 K by Tristar 3020 specific surface meter of Micro-Meritics, USA, and the Brunauer-Emmett-Teller method (BET) was used to calculate the specific surface area. The surface structure of the sample was analyzed by AXIS ULTRA DLD X-ray photoelectron spectroscopy (XPS) from Shimadzu, Japan. Monochromatic Al K α was used as light source and C 1s (284.6 eV) was used as reference to correct all electron binding energies.

Fabrication and Measurement of Humidity Sensors: The humidity sensing performance of the sensor was tested by TH2829A LCR instrument of Changzhou Tonghui Electronics Co. Ltd. The fastest sampling interval of the machine is 100 ms. The fabrication of the sensor and the test process of humidity sensitive properties were as follows: a small amount of Ho_2O_3 sample was put into agate mortar. After full grinding, the powder was uniformly dispersed in terpineol to form a viscous paste. Then, it was evenly coated with a small brush on the Au interdigitated electrode with a spacing of 50 μm on Al_2O_3 ceramic substrate (9.4 mm×9.4 mm×0.38 mm). which was heat treated in muffle furnace at 300℃ for 1 h to obtain Ho_2O_3 humidity sensor device. The prepared sensing element is shown in Fig. S1a, and the surface structure of the element can be tested by SEM as shown in Fig. S1b. It shows that the material still retains the original morphological structure after grinded, coated and heat treated. The saturated salt solution of LiCl, $MgCl_2$, $Mg(NO_3)_2$, NaCl, $Pb(NO_3)_2$ was prepared in a glass container and placed for at least 24 h to obtain 11.30%, 32.78%, 54.38%, 75.29% and 95.00% humidity atmosphere of relative humidity (RH). The solution preparation and test environment were carried out at 25°C ± 1°C. The TH2829A LCR test system was used to control the test parameters and record the real-time parameters of the sensor. During the test, the impedance value measured at the initial humidity is recorded as Za, the impedance value measured at the measured humidity is recorded as Zg, and the sensitivity is R=Za/Zg. The response-recovery time is the time of 90% change of the corresponding impedance value. The specific test device flow chart is shown in Fig. S2.

Application Test of Humidity Sensor: In the application performance test of Ho_2O_3 nanomaterials, taking respiration as an example, human beings breathe at a rate of 12-20 times per minute during normal breathing, which requires water molecules on the surface of the sensing material responsible for monitoring human respiration to complete adsorption and desorption quickly during each respiration cycle. Therefore, the material must have a fast response time and recovery time so that it can better monitor each respiratory change of the cycle in real time. So, the ultra-thin porous Ho_2O_3 nanomaterial is used as the sensing material of the humidity sensor, and the fabrication process of the sensor is the same as the previous method. The test was carried out with the TH2829A LCR instrument of Changzhou Tonghui Electronics Co. Ltd.

The humidity sensor was fixed in the breathing valve on one side of the Chengkai N95 double-way valve mask sold in the market, and tested under the air condition of 25°C, 15 ±5% RH (the test method is shown in Fig. S3.). In the test, although the sensor has a very large sensitivity and a large order of magnitude change at the working frequency of 300 Hz, the humidity of each exhaled gas of the human body is not guaranteed to be the same humidity in the process of respiratory monitoring. Therefore, at the working frequency of 300 Hz, the maximum and minimum impedance values of the sensor during the cycle can not reach the same measuring platform line. In order to, the working frequency of the sensor was adjusted to 30k Hz when measuring breathing. At this working frequency, the maximum and minimum impedance values can be approximately close to the same platform point in the process of monitoring respiration by the sensor.

In the measurement of humidity on the fingertip, human body surface humidity and efficacy test of moisturizing products, the 3D printing technology was used to make a small testing device as shown in Fig. S4. The distance between the forked finger electrode and the upper hole was 0.5 mm, 1 mm, 2 mm, 3 mm, 5 mm respectively. Before testing, the forked finger electrode was put into the slot, fixed by the test clip and connected to the LCR tester. During the test, the upper end opening of the 3D printed small device was fastened to the body surface to be measured. (The specific test methods see Support Information Video.)

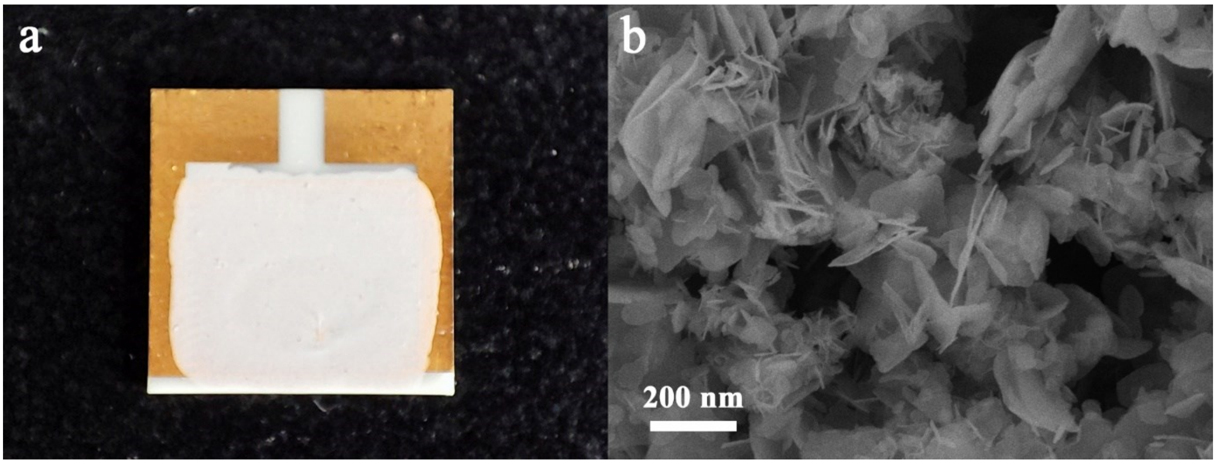

Fig. S1. a) The image of the sensor element after preparation. b) SEM image of interdigital electrode surface after preparation.

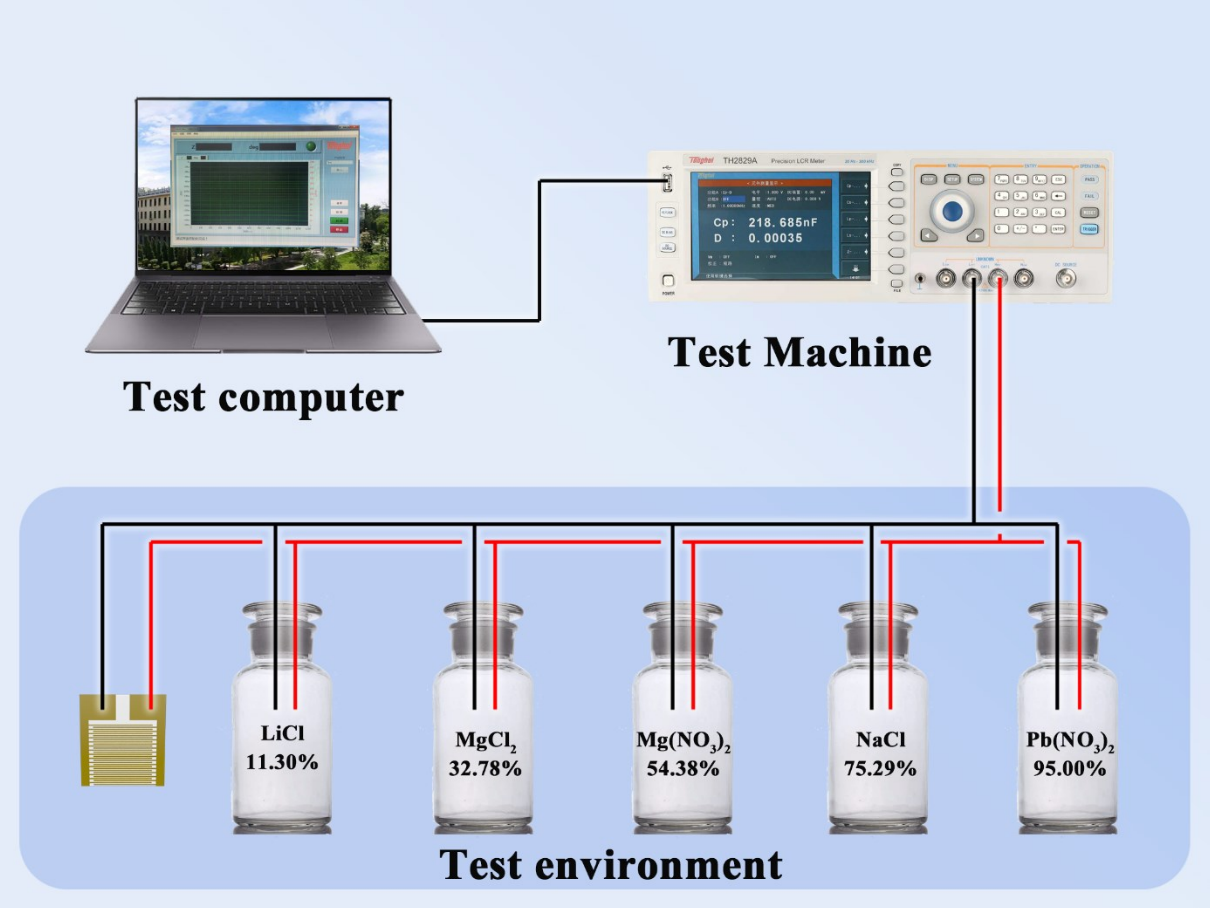

Fig. S2. Humidity sensor test pattern.

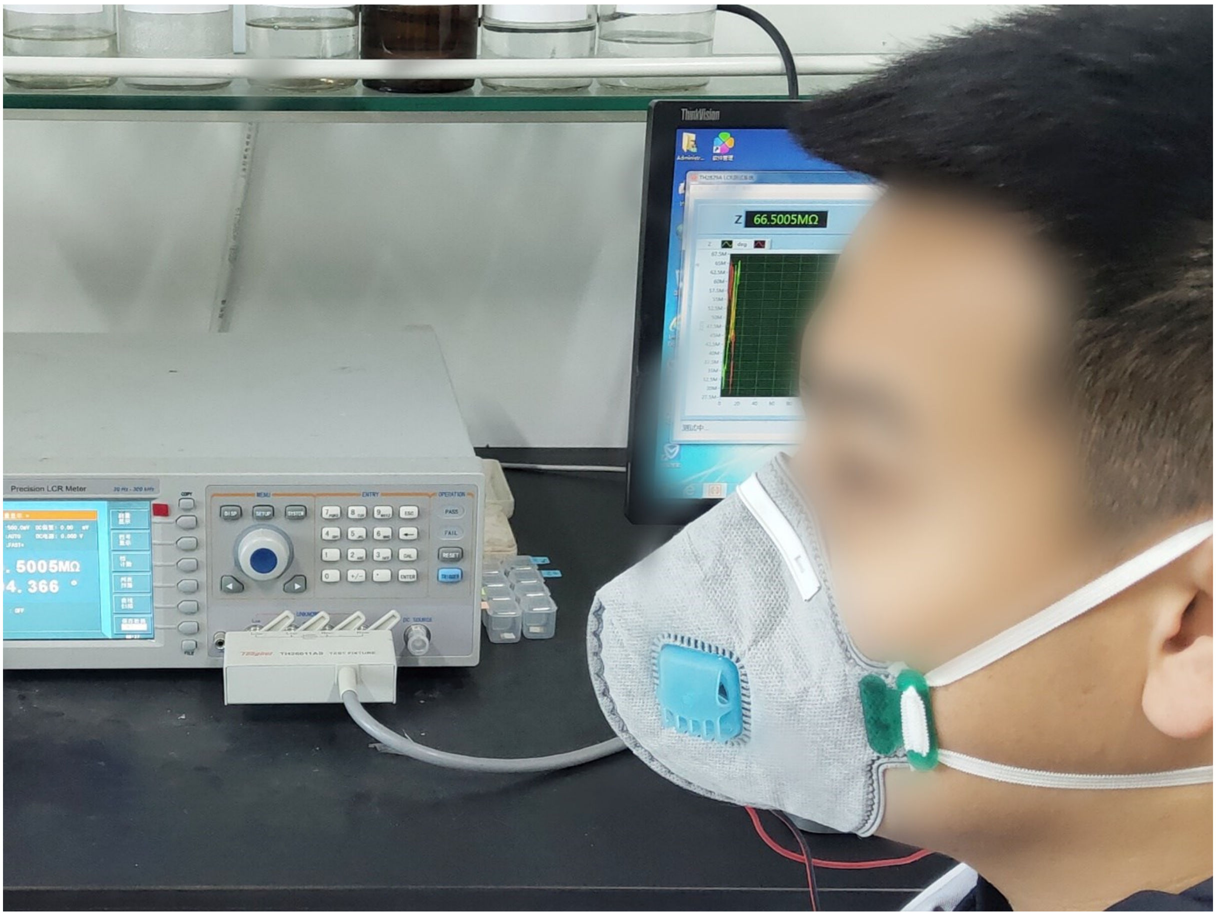

Fig. S3. Simulation test method of breathing test device.

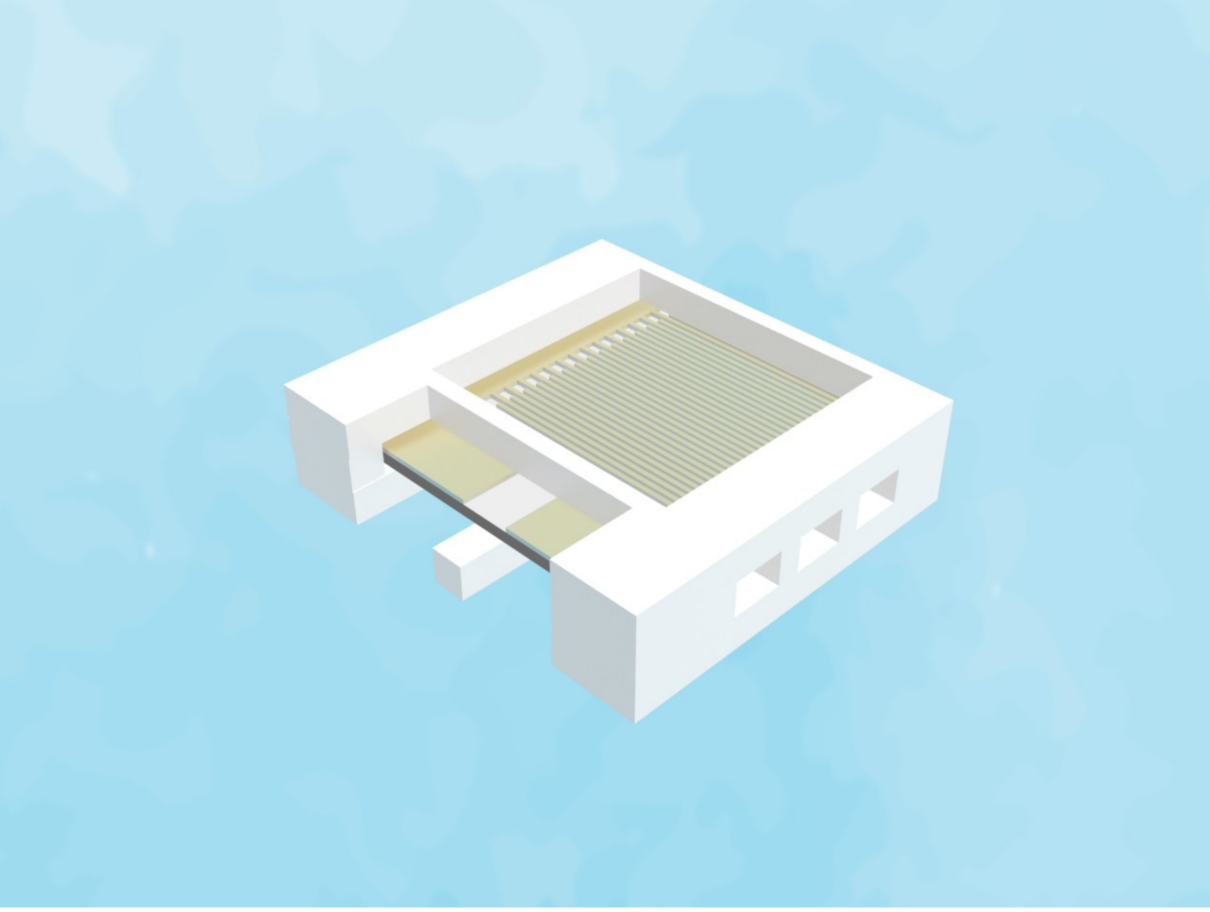

Fig. S4. A small test device based on 3D printing technology.

Part II: Morphology Control of the Ho_2O_3 Nanostructures

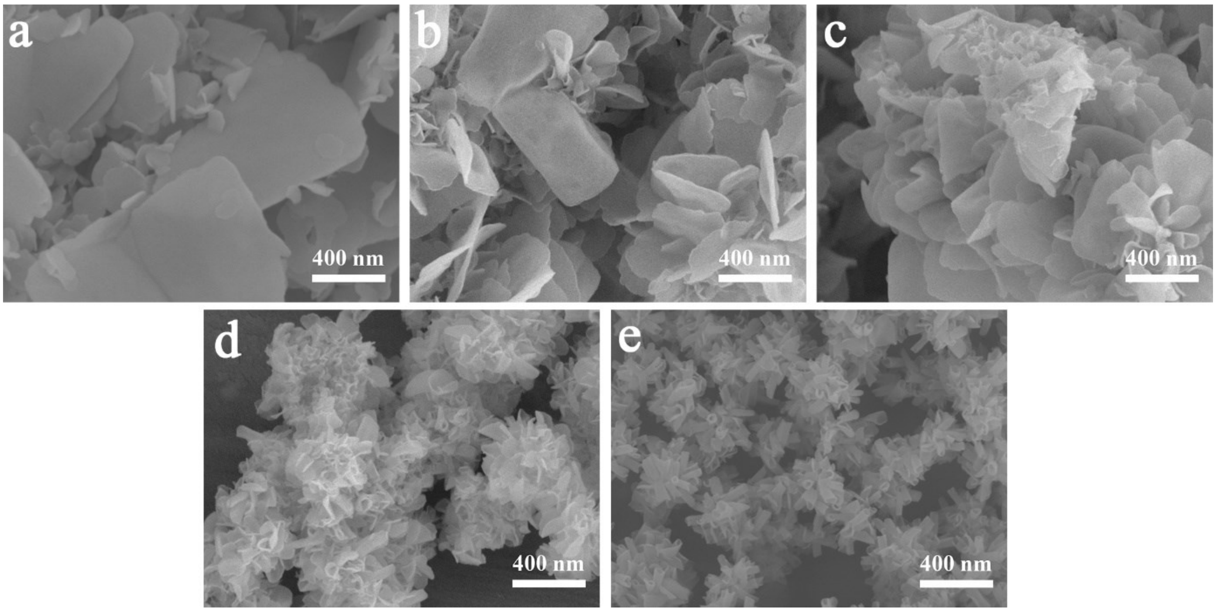

Fig. S5. The SEM images of the samples when the volume ratio of alcohol to DI water in the solution is a) 19:6, b) 20:5, c) 21:4, d) 22:3, e) 23:2.

On the basis of keeping the other synthesis conditions unchanged, the volume ratio of alcohols to DI water in the solution was increased and the morphology of the products was observed. Fig. S5a-e show the SEM images of the precursors of when the volume ratio of alcohol to DI water is 19:6, 20:5, 21:4, 22:3 and 23:2, respectively. As the volume ratio of alcohols to DI water in the solution gradually increases, the nanosheets are gradually rolled into a tubular structure to form nanotubes.

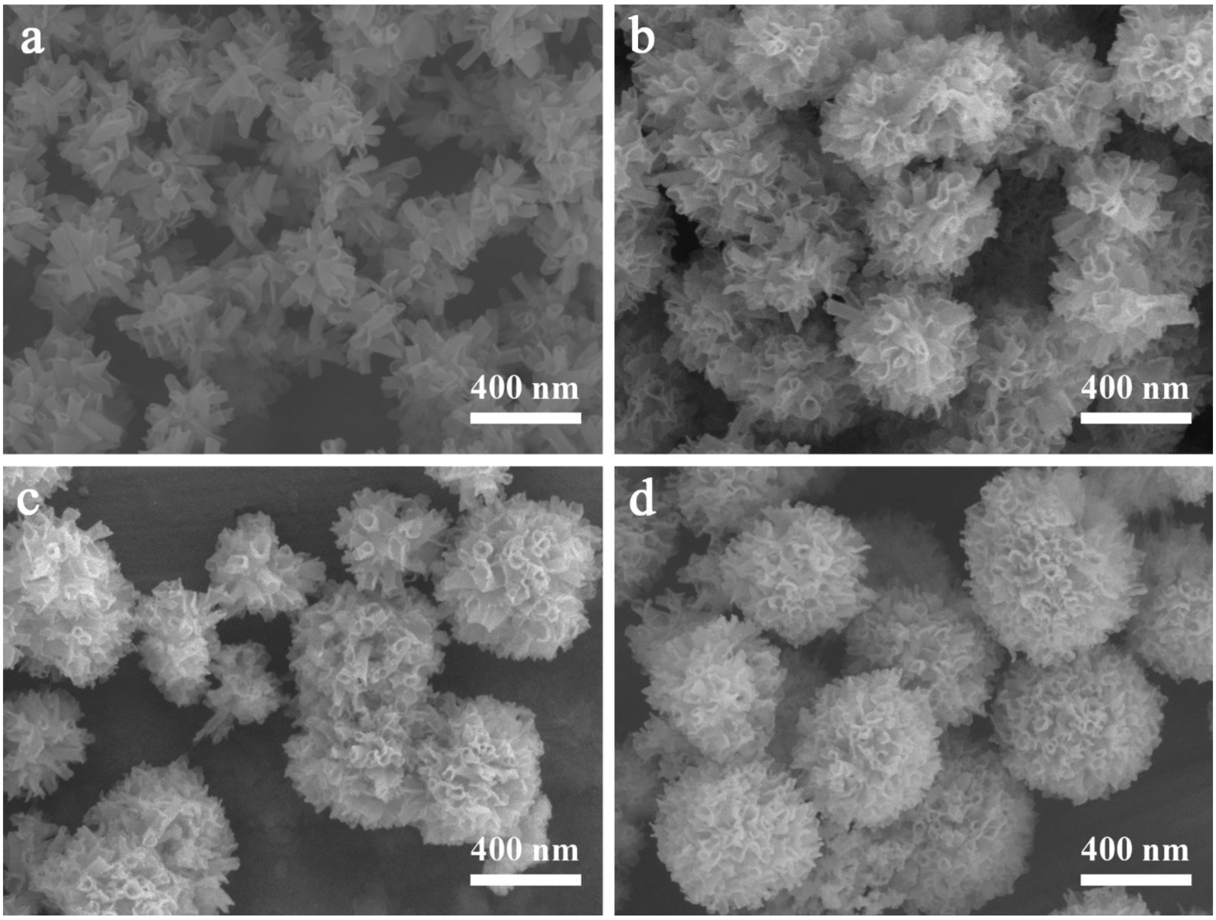

Fig. S6. The SEM images of the samples when the urea content in the solution is a) 1 mmol, b) 2 mmol, c) 3 mmol, d) 4 mmol.

On the basis of keeping other conditions unchanged, the amount of urea in the reaction system was gradually changed. Fig. S6a-d are SEM images of the precursors when the amount of urea is 1 mmol, 2 mmol, 3 mmol and 4 mmol, respectively. Compared with the tubular structure with urea addition of 1 mmol with the gradual increase of the addition amount of urea, the nanotubes gradually self-assemble into a spherical structure, the separate tubular structure gradually decreased until the final urea addition amount is 4 mmol, and the sample completely exhibits the appearance of a nanotube self-assembled sphere. The pH value of the solution after the reaction was measured by pH meter. When the amount of urea is 1 mmol, 2 mmol, 3 mmol, 4 mmol, the pH value of the solution after reaction is 8.79, 9.72, 9.89, 10.01, that is, the alkalinity of the solution is gradually enhanced.

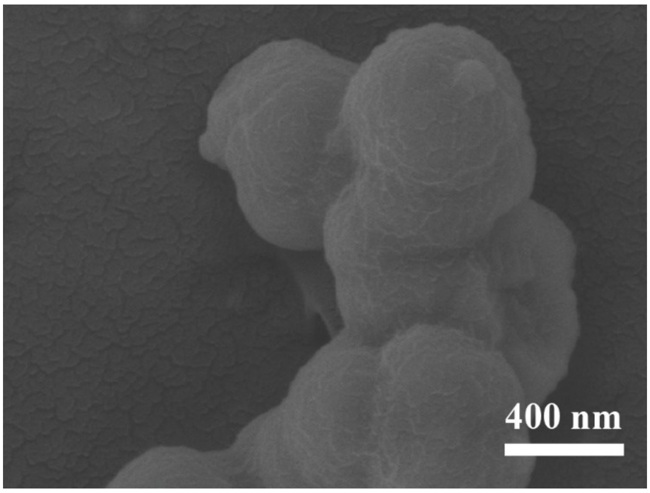

Fig. S7. SEM image of samples prepared without water in the system.

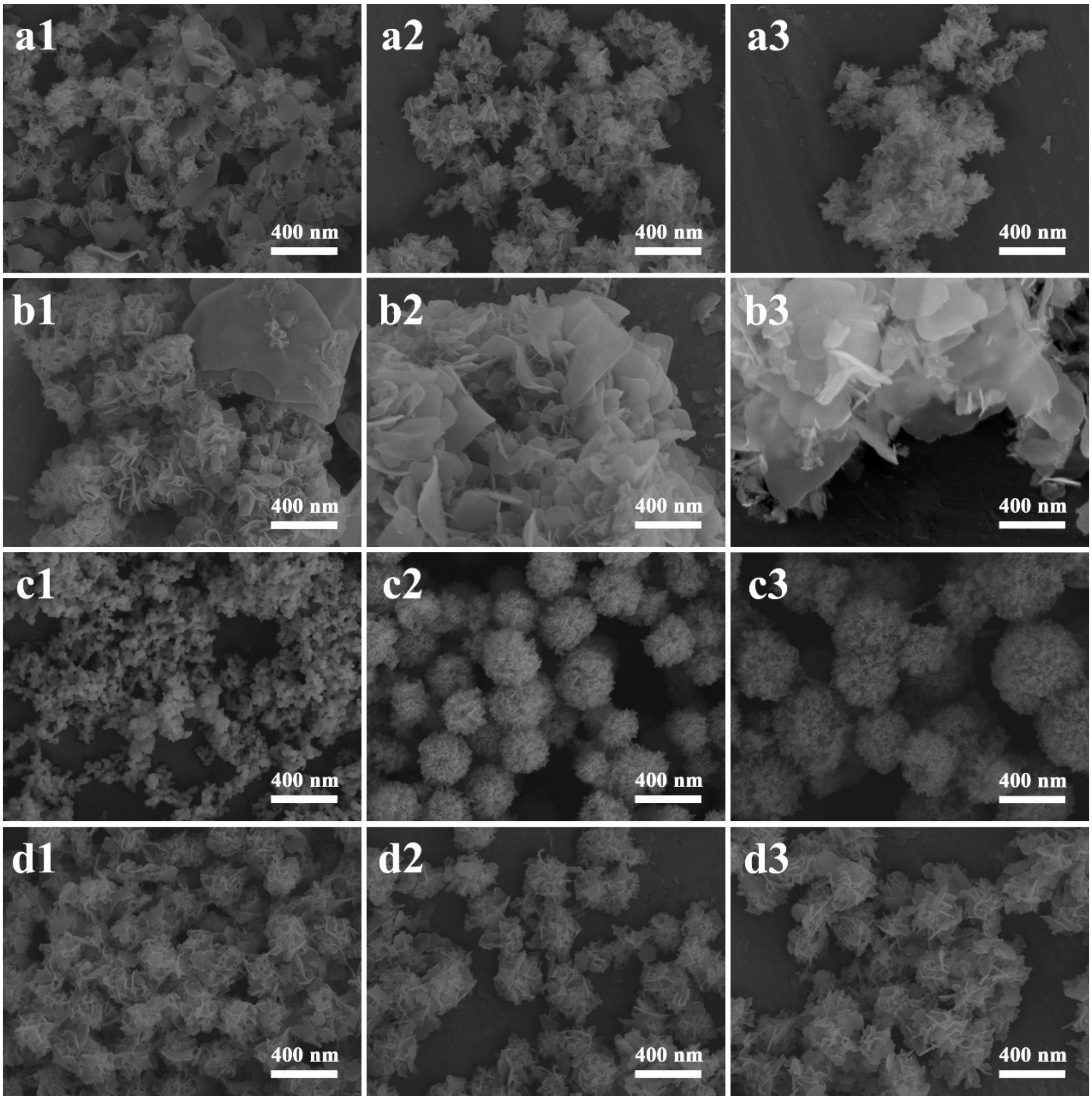

Fig. S8. SEM images of Ho_2O_3 (a1-a3) NT, (b1-b3) NS, (c1-c3) NTS, (d1-d3) NSS under reaction time of (a1-d1) 2h, (a2-d2) 4h, (a3-d3) 8h.

It can be found from the tests that the nanotube structure, nanosheet structure and nanosheet spherical structure materials can show the sheet structure at 2 h of reaction, which may be due to the small amount of water in the system. The water adsorption and covering of water film on the surface of the material will inhibit the growth of the material in the Z-axis direction and thus grow the lamellar structure in the XY direction. And some tubular structures will be formed, via some sheets curling at reaction of 2 h, which is caused by the solvothermal environment of the tubular structure with too little water content. This results in the amount of water molecules not enough to be completely adsorbed on the surface of the material. As the reaction time increases, the water molecules are not enough to reduce the great energy on the surface of the material, therefore, the sheets will curl to form a tubular structure. At the same time, the addition of urea leads to the enhancement of alkalinity in the solution, which promotes the nucleation rate of the material in the solvothermal reaction and simultaneously generates a large number of nuclei and aggregates to form a cluster structure. So, the lamellar spherical and tubular spherical structures will grow more easily in aggregation or clusters at reaction time of 2 h, compared with the lamellar and tubular structures.

Part III: The optimum calcination temperature of Ho_2O_3 nanomaterials and the change process from precursor to Ho_2O_3

In order to determine the conversion process of the sample from the precursor to Ho_2O_3 nanomaterials and the optimal calcination temperature, TG (Fig. S9) and FT-IR (Fig. S10) characterization and analysis were performed. The samples were also characterized by XRD before calcination and at different calcination temperatures (Fig. S11). At the same time, in order to ensure that the morphology of the samples can be better preserved after calcination, the samples of Ho_2O_3 nanomaterials precursor calcined in air atmosphere at 600°C (Fig. S12) and 700°C (Fig. S13) were characterized by SEM. Finally, the optimum calcination temperature of Ho_2O_3 nanomaterials was determined to be 600°C. (Except for the special mentions below, the Ho_2O_3 nanomaterials all indicate that their calcination temperature is 600°C.)

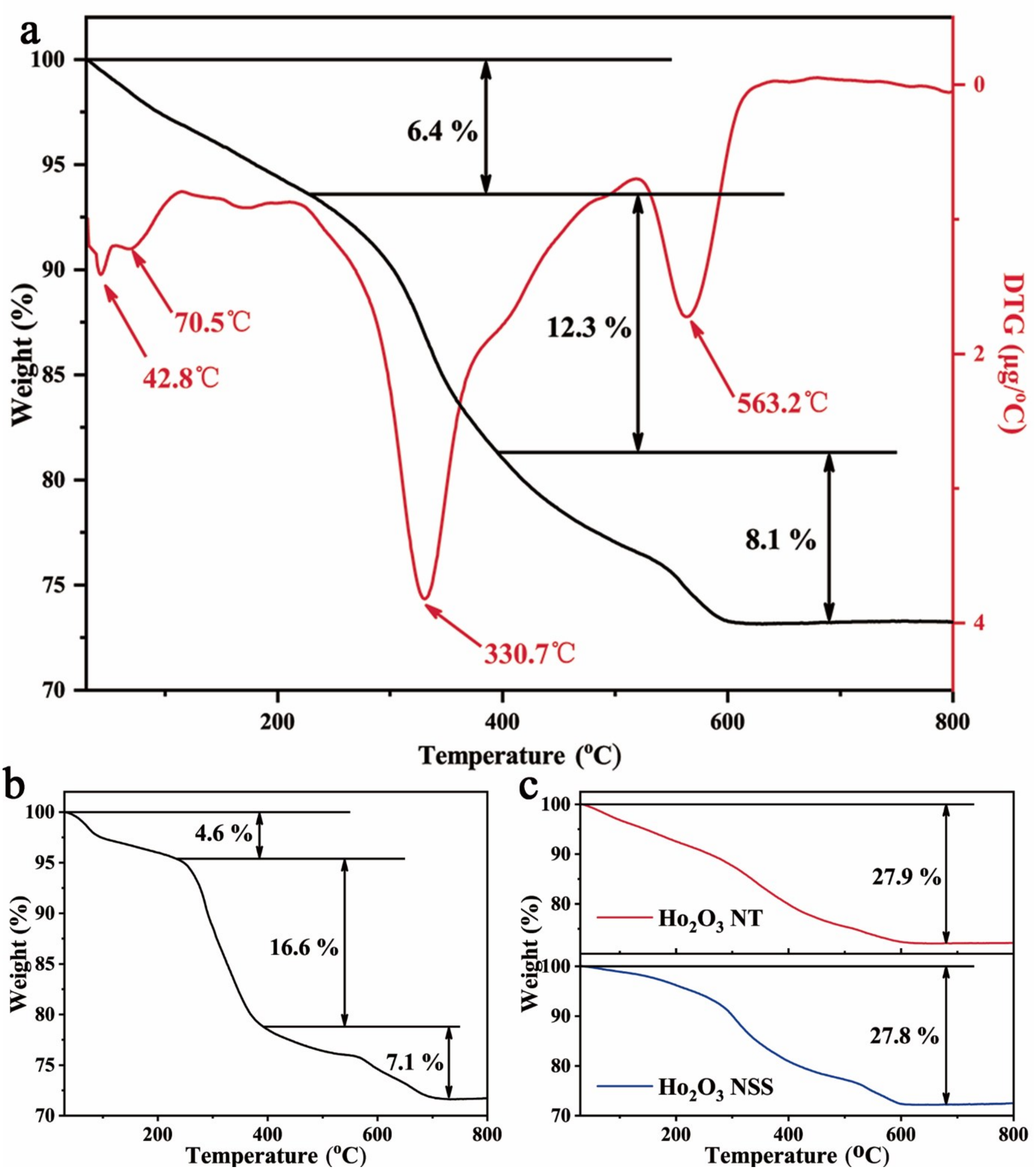

Fig. S9. TG-DTG curves of Ho_2O_3 precursors: a) NTS, b) NS, c) NT and NSS.

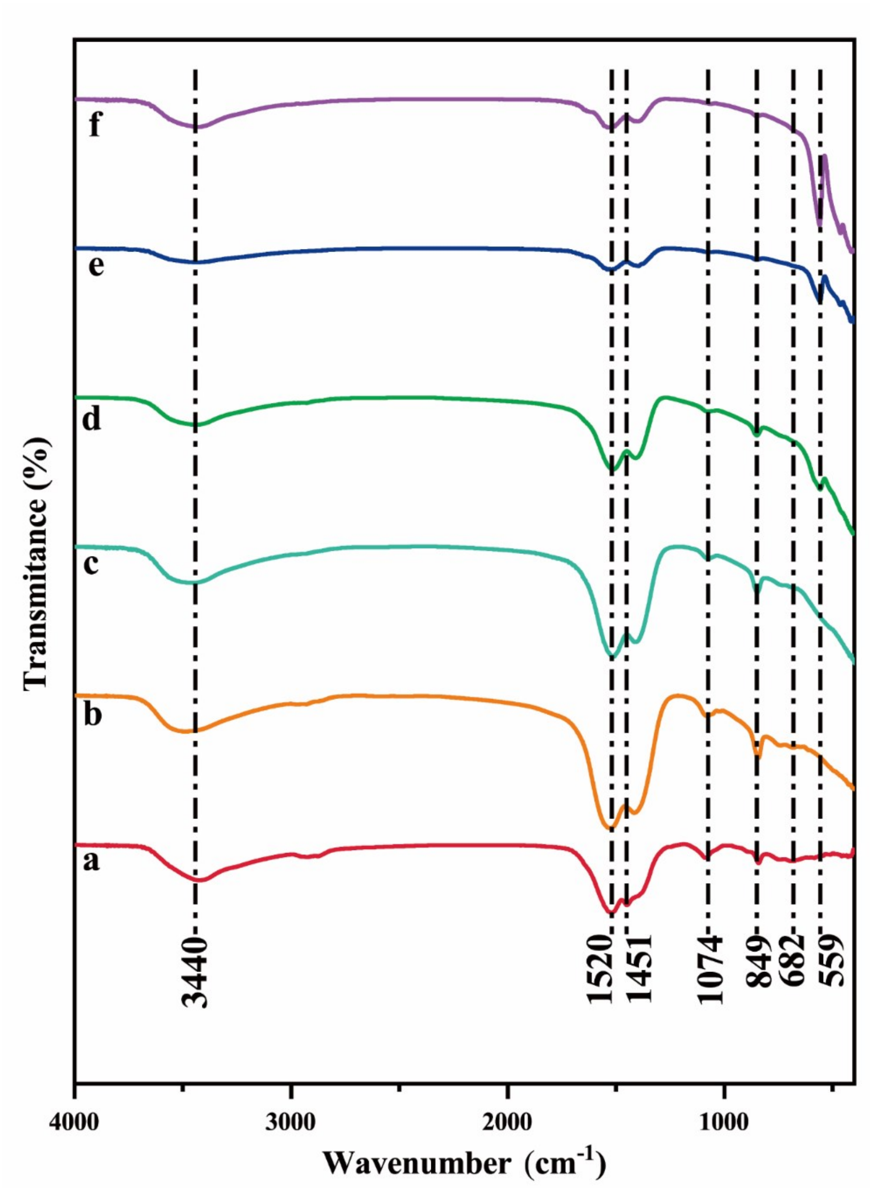

Fig. S10. FT-IR spectra of Ho_2O_3 NTS: a) Precursor, products after calcined at b) 300°C, c) 400°C, d) 500°C, e) 600°C, f) 700°C.

The TG-DTG curves of the Ho_2O_3 NTS precursor is shown in Fig. S9a Through the weight loss curve in the figure, it can be found that there are mainly three weight loss processes from the precursor to Ho_2O_3.[1,2]

In the first stage, the weight loss in 30-228°C, and the endothermic peak on the corresponding DTG curve is 70.5°C. The infrared spectra of the Ho_2O_3 NTS can be seen (Fig. S10a). In the infrared spectrum of the precursor, the peaks in the sample 3440 cm^{-1}, (1520 cm^{-1}, 1451 cm^{-1}), 1074 cm^{-1}, 849 cm^{-1} and 682 cm^{-1} can be attributed to $\nu(OH^-)$, $\nu_{as}(CO_3^{2-})$, $\nu_s(CO_3^{2-})$,γ (CO_3^{2-}) and Ho-O-H, respectively.[3] At the same time, Due to the formation of a large number of

CO_3^{2-} and OH^-, in reaction (b) and reaction (c), so we speculate that the reaction of solvothermal is:[4]

$$CO(NH_2)_2 + H_2O \rightarrow 2NH_3 + CO_2 \qquad a)$$

$$2NH_3 + 2H_2O \rightarrow 2NH_4^+ + 2OH^- \qquad b)$$

$$CO_2 + H_2O \rightarrow 2H^+ + CO_3^{2-} \qquad c)$$

$$Ho^{3+} + OH^- + CO_3^{2-} \rightarrow HoOHCO_3 \qquad d)$$

Therefore, the precursor may be $HoOHCO_3$, which is consistent with the peak produced by infrared spectrum. At this stage, the adsorbed water on the sample surface was mainly removed from $HoOHCO_3$, and the mass loss was about 6.4wt%.

In the second stage, the weight loss in 228-394°C, and the endothermic peak on the DTG curve is 330.7°C. As shown in Fig. S10, In the infrared spectrum of the samples after calcined at 300°C and 400°C, the peaks in the sample 3440 cm^{-1}, (1520 cm^{-1},1394 cm^{-1}), 1074 cm^{-1} and 850 cm^{-1} can be attributed to $\nu(OH^-)$, $\nu_{as}(CO_3^{2-})$, $\nu_s(CO_3^{2-})$ and $\gamma(CO_3^{2-})$, respectively.[5] It is speculated that at this time, the $HoOHCO_3$ in the precursor removes a molecule of H_2O and a molecule of CO_2, to form $Ho_2O_2CO_3$, and the main weight loss is 12.3%.

In the third stage, the weight loss in 394-600°C, and the endothermic peak on the DTG curve corresponding to this stage is 563.2°C. As shown in Fig. S10, the characteristic peak produced by Ho-O bond gradually appears at 559 cm^{-1} after calcination at 500°C, and the intensity of the peak increases with the increase of calcination temperature. In this stage, the thermogravimetric curve no longer changes after $Ho_2O_2CO_3$ removes a molecule of CO_2, with a mass loss of about 8.1 wt%, indicating that the precursor has been completely transformed into Ho_2O_3 at 600°C.

Fig. S9b shows the TG curve of the precursors of Ho_2O_3 NS nanomaterials, and the main weight loss process is consistent with that of the Ho_2O_3 NTS. However, in the third stage of weightlessness, the lamellar morphology will produce a stack of porous structures and lamellar structures, so higher temperature is needed to reach the weightlessness platform. The TG curves of the Ho_2O_3 NT and Ho_2O_3 NSS (Fig. S9c) precursors show that the weight loss process is basically consistent with the precursor weightlessness curve of Ho_2O_3 NTS morphology.

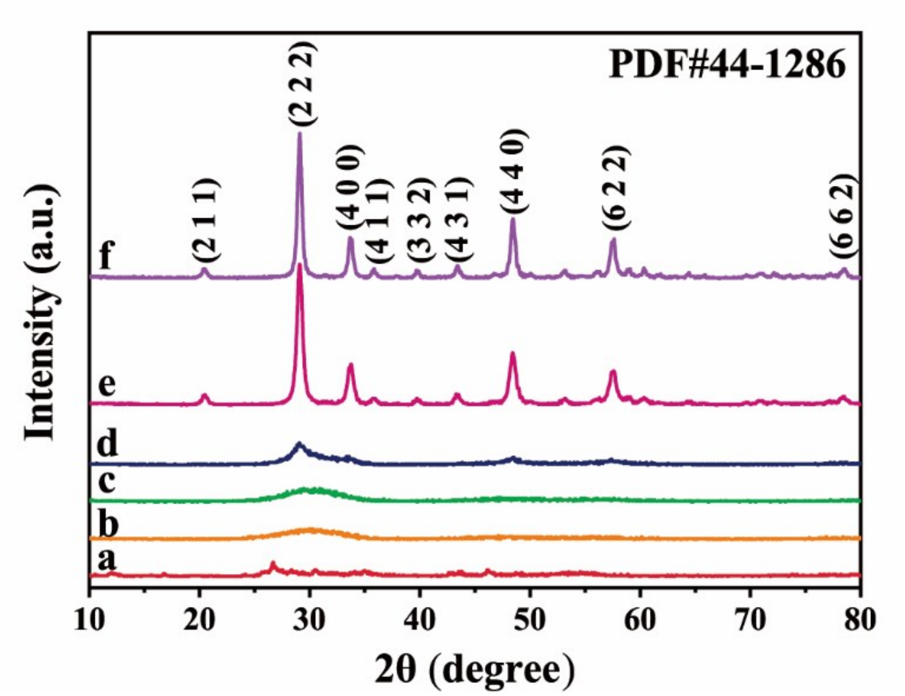

Fig. S11. XRD patterns of precursor (a) and calcined products at 300°C (b), 400°C (c), 500°C (d), 600°C (e) and 700°C (f).

Fig. S11 shows the XRD patterns of Ho_2O_3 NTS nanomaterial before calcination and at different calcination temperatures of the materials. It can be obtained from the test results that the crystallinity of the product is poor before calcination and the calcination temperature is within 400°C. When the calcination temperature is 500°C, the material exhibits the (2 2 2) characteristic peak of Ho_2O_3 material (PDF#44-1286), but the crystallinity is still relatively weak. With the further increase of the calcinnation temperature showing more crystalline directional diffraction peak appear and the diffraction peaks gradually become stronger, the better crystallinity of the material after calcined at high temperature. However, when the calcination temperature is increased to 700°C, the morphology of the precursor can not retained. Therefore, high temperature calcination can gradually improve the purity and crystallinity of Ho_2O_3 material.

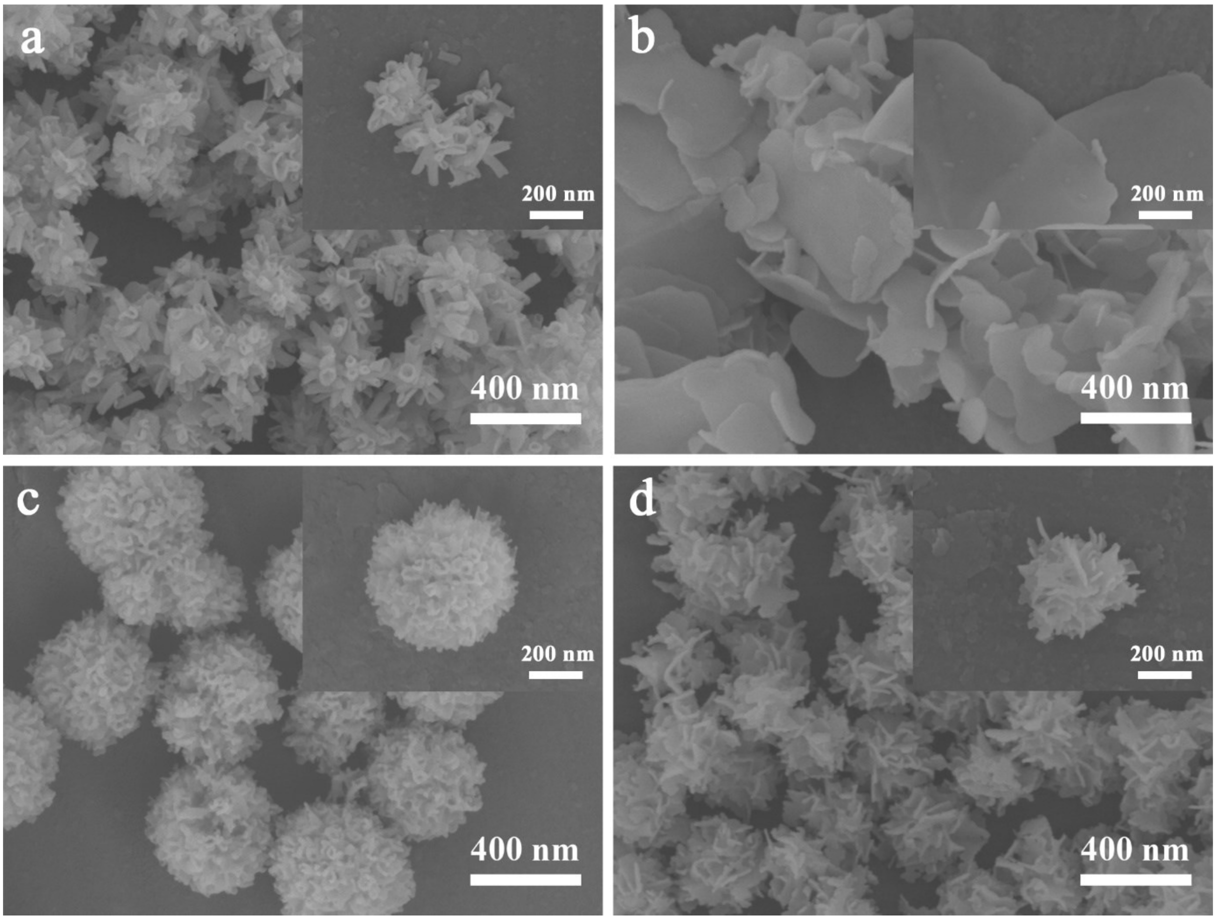

Fig. S12. SEM images of the Ho_2O_3 a) NT, b) NS, c) NTS, d) NSS after calcined at 600°C.

From the SEM image (Fig. S12) of the samples calcined at 600°C, it can be seen that the morphology of Ho_2O_3 nanomaterials with four morphologies calcined at 600°C has no obvious change compared with the corresponding precursors.

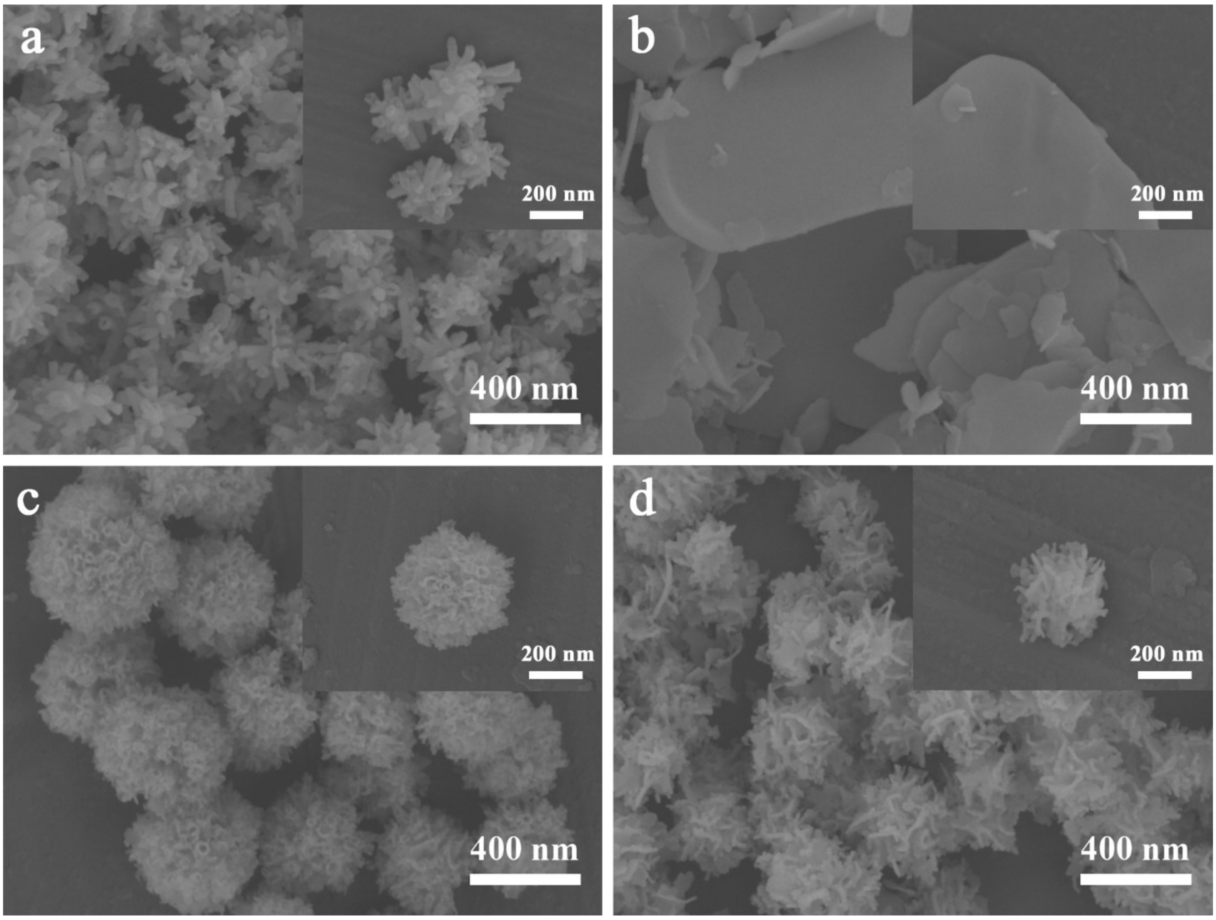

Fig. S13. SEM images of the Ho_2O_3 a) NT, b) NS, c) NTS, d) NSS after calcined at 700°C.

After calcination at 700°C (Fig. S13), the morphologies of Ho_2O_3 NT, NTS and NSS all show a trend of melting and aggregation, and the sample sizes decrease. The morphology of the sample can not be well preserved. Therefore, Ho_2O_3 nanomaterials were prepared by calcination at 600°C in air atmosphere.

Part IV: Figures and Tables

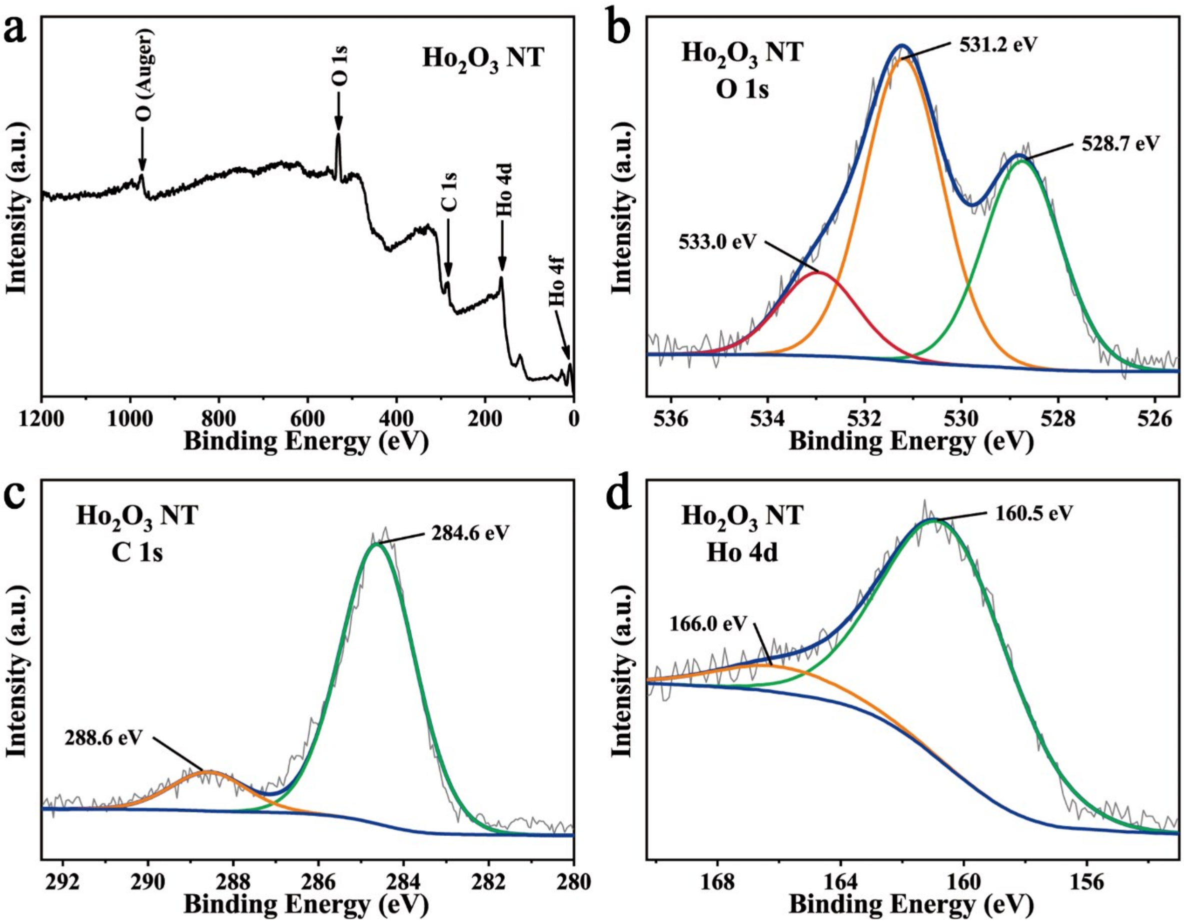

Fig. S14. a) XPS survey spectrum and high-resolution elemental, b) O 1s, c) C 1s and d) Ho 4d spectra of the Ho_2O_3 NT after calcined at 600°C.

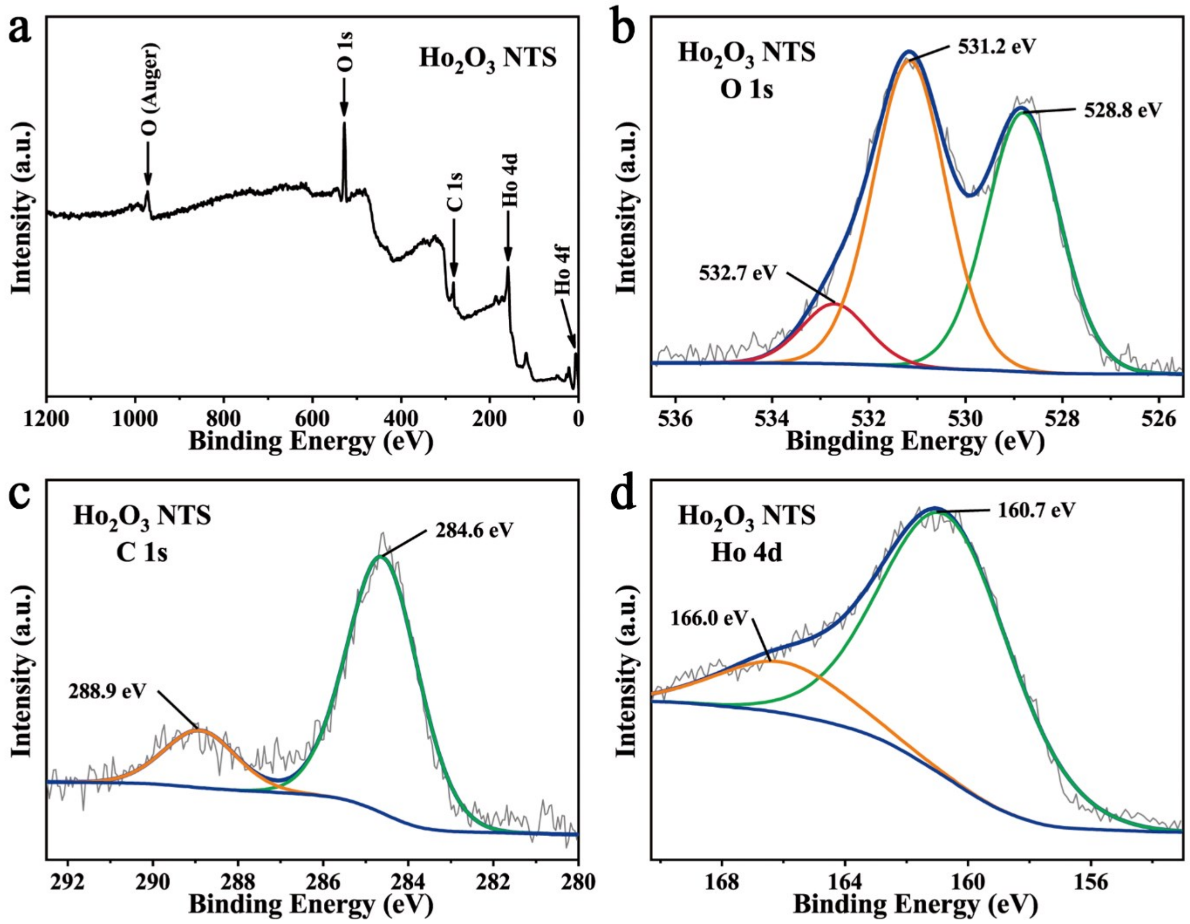

Fig. S15. a) XPS survey spectrum and high-resolution elemental, b) O 1s, c) C 1s and d) Ho 4d spectra of the Ho_2O_3 NTS after calcined at 600°C.

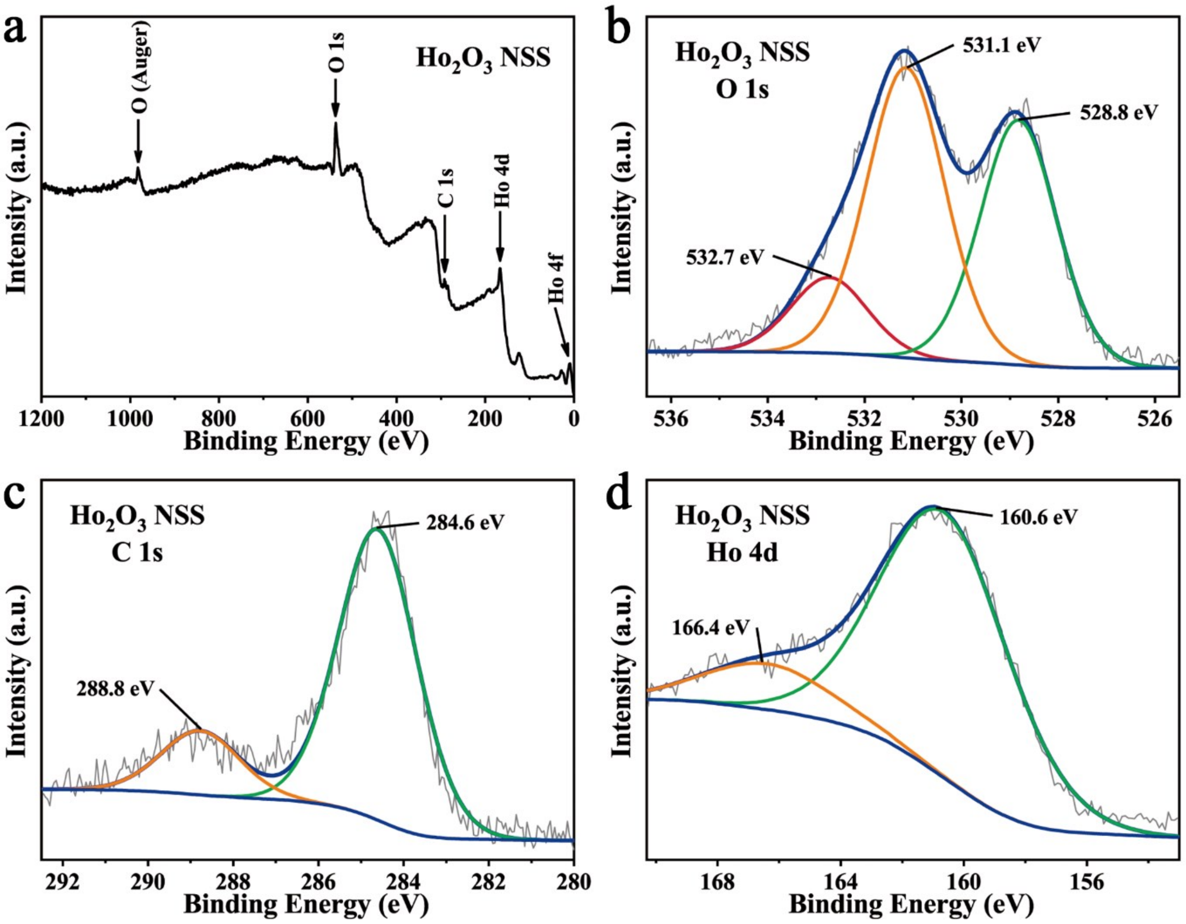

Fig. S16. a) XPS survey spectrum and high-resolution elemental, b) O 1s, c) C 1s and d) Ho 4d spectra of the Ho_2O_3 NSS after calcined at 600°C.

Table S1. Analysis of O content in XPS

	Lattice oxygen		Hydroxyl oxygen		Carbonate radical	
	Peak position	Percentage /%	Peak position	Percentage /%	Peak position	Percentage /%
Ho_2O_3 NT	528.7	34.9	531.2	51.0	533.0	14.1
Ho_2O_3 NS	529.0	14.5	531.3	45.9	532.9	39.6
Ho_2O_3 NTS	528.8	41.8	531.2	49.5	532.7	8.7
Ho_2O_3 NSS	528.8	39.7	531.1	48.0	532.7	12.3

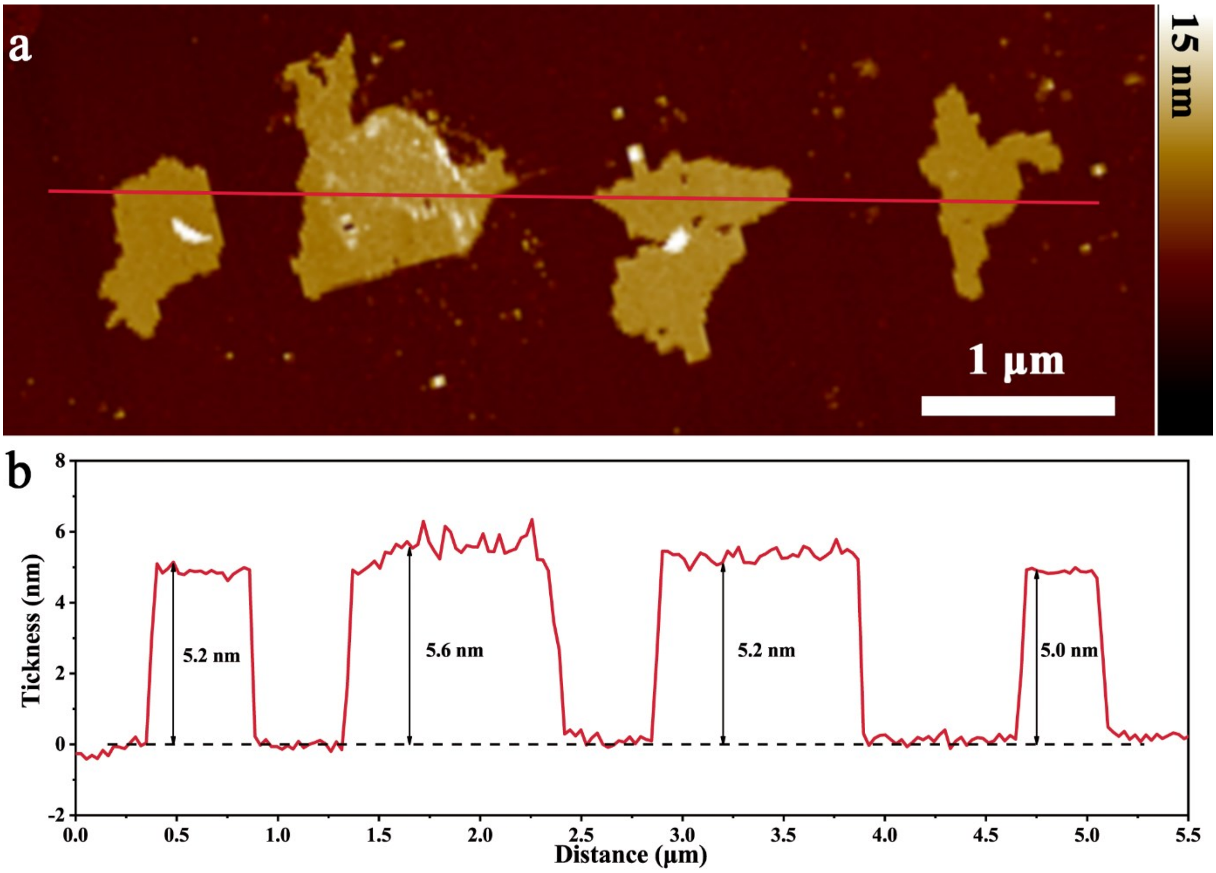

Fig. S17. AFM images of Ho_2O_3 nanosheet.

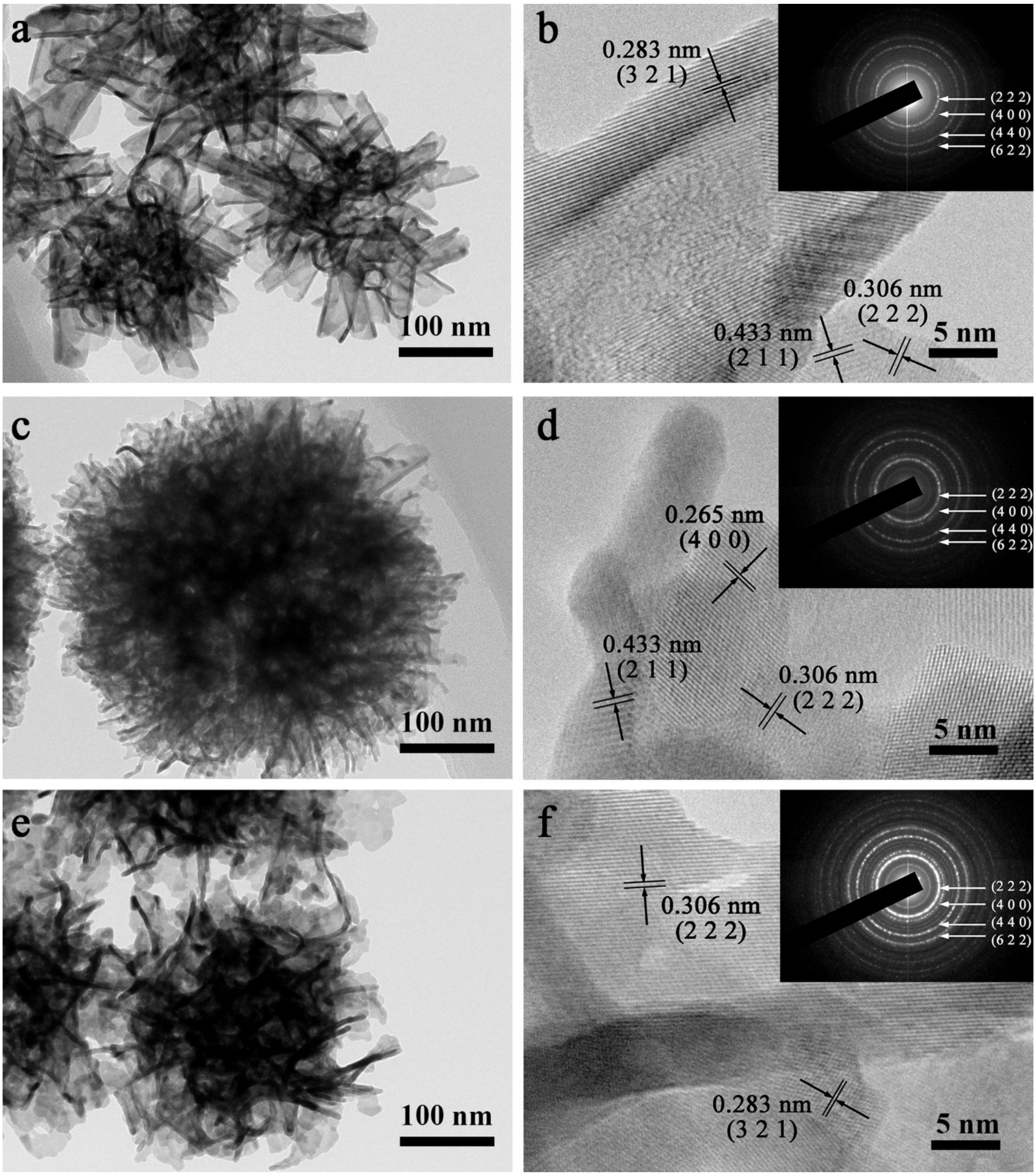

Fig. S18. a. c. e) TEM images of Ho_2O_3 NT, NTS, NSS after calcined at 600°C, b. d. f) HRTEM images of Ho_2O_3 NT, NTS, NSS (the inset is the corresponding SAED pattern) after calcined at 600°C.

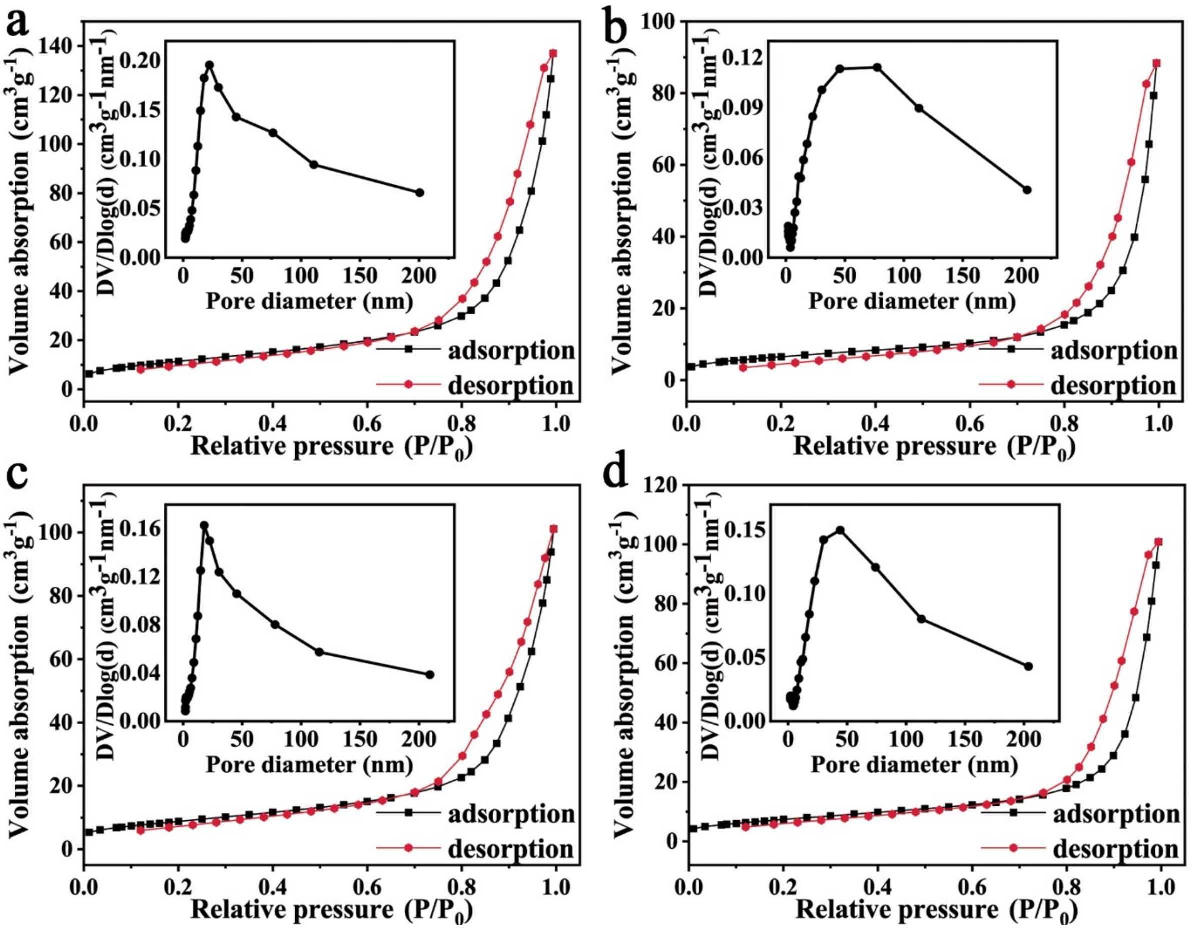

Fig. S19. The nitrogen adsorption-desorption isotherms of Ho_2O_3 a) NT, b) NS, c) NTS, d) NSS after calcined at 700°C. (The inset is the BJH pore size distribution curve)

After calcination at 700°C, the adsorption-desorption isotherm curves of the four samples are determined as type IV isotherms with H3 hysteresis loops. According to the BET method, the specific surface area of the sample is obtained. The specific surface areas of Ho_2O_3 NT (Fig. S19a), NS (Fig. S19b), NTS (Fig. S19c), NSS (Fig. S19d) are 42.2, 23.7, 32.1, 27.3 m^2·g^{-1}, respectively. Compared with the samples calcined at 600°C, the specific surface area decreases, which is also related to the collapse of the morphology of the samples calcined at 700°C.

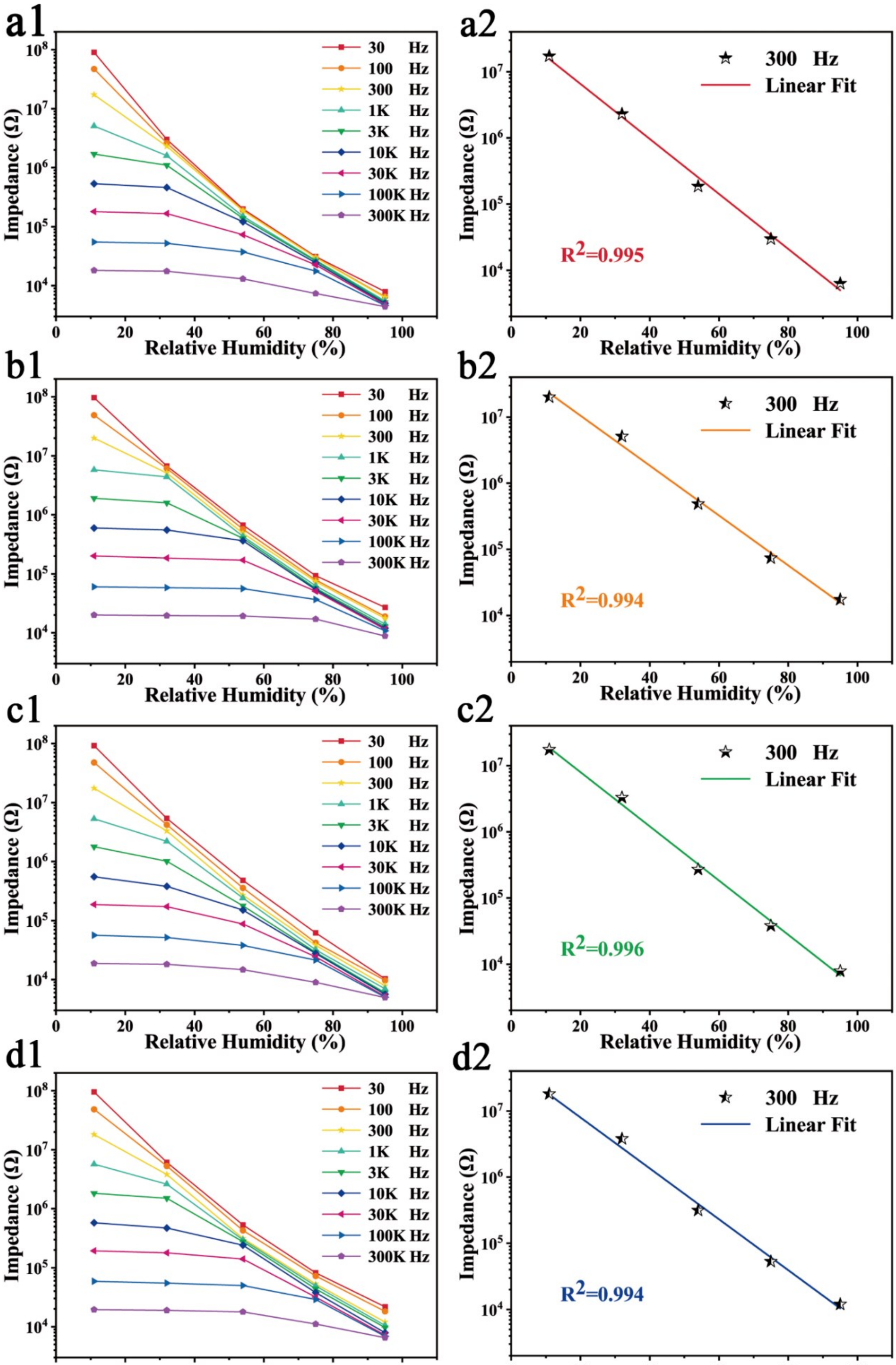

Fig. S20. Impedance of Ho_2O_3 a) NT, b) NS, c) NTS, d) NSS humidity sensors to different humidity at different frequencies (1) and linear relationship of impedance to humidity at 300 Hz (2).

Fig. S20 (a1. b1. c1. d1) shows the impedance changes of Ho_2O_3 nanomaterials with four morphologies at different operating frequencies (30 Hz, 100 Hz, 300 Hz, 1k Hz, 3k Hz, 10k Hz, 30k Hz, 100k Hz, 300k Hz) and different humidity (11.30%, 32.78%, 54.38%, 75.29%, 95.00% RH). It can be clearly found from the figure that the impedance values of the samples with four morphologies decrease with the increase of humidity at any frequency. At the same humidity, the higher the measurement frequency is, the lower the corresponding impedance value is. Under the condition of high frequency, the change of impedance is smaller than that of low frequency. This is because at high frequency, the polarization speed of water is slower than the direction of electric field, and the electric field can not maintain the induced polarization of water vapor adsorbed in Ho_2O_3 nanomaterials.[6,7] However, under the condition of low frequency, the sample can not reach a stable impedance value in low humidity environment, and the impedance value in different humidity is difficult to show a good linear relationship. Finally, 300 Hz is selected as the best working frequency, and the impedance changes of NT and NTS can reach four orders of magnitude in the whole range of RH, and the impedance changes of NS and NSS can also reach nearly four orders of magnitude. As can be seen from Fig. S20 (a2, b2, c2, d2), the linear fit of the four samples are all greater than 0.99 under five humidity conditions.

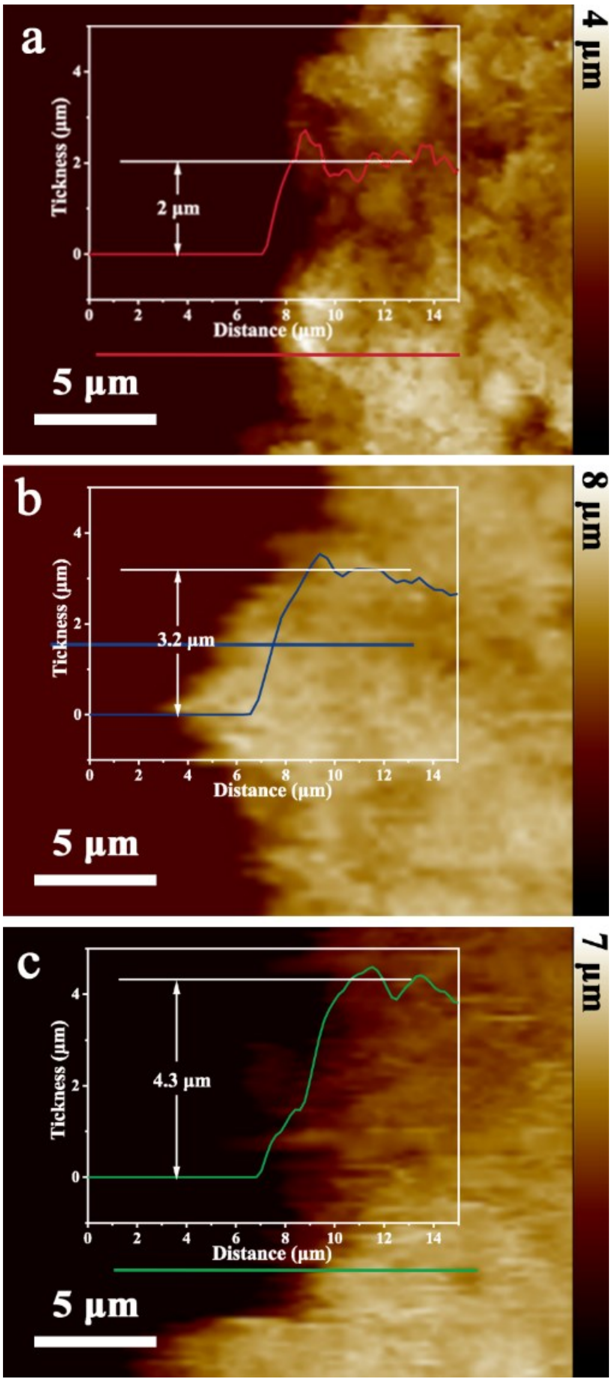

Fig. S21. AFM images of humidity sensors with three different film thicknesses.

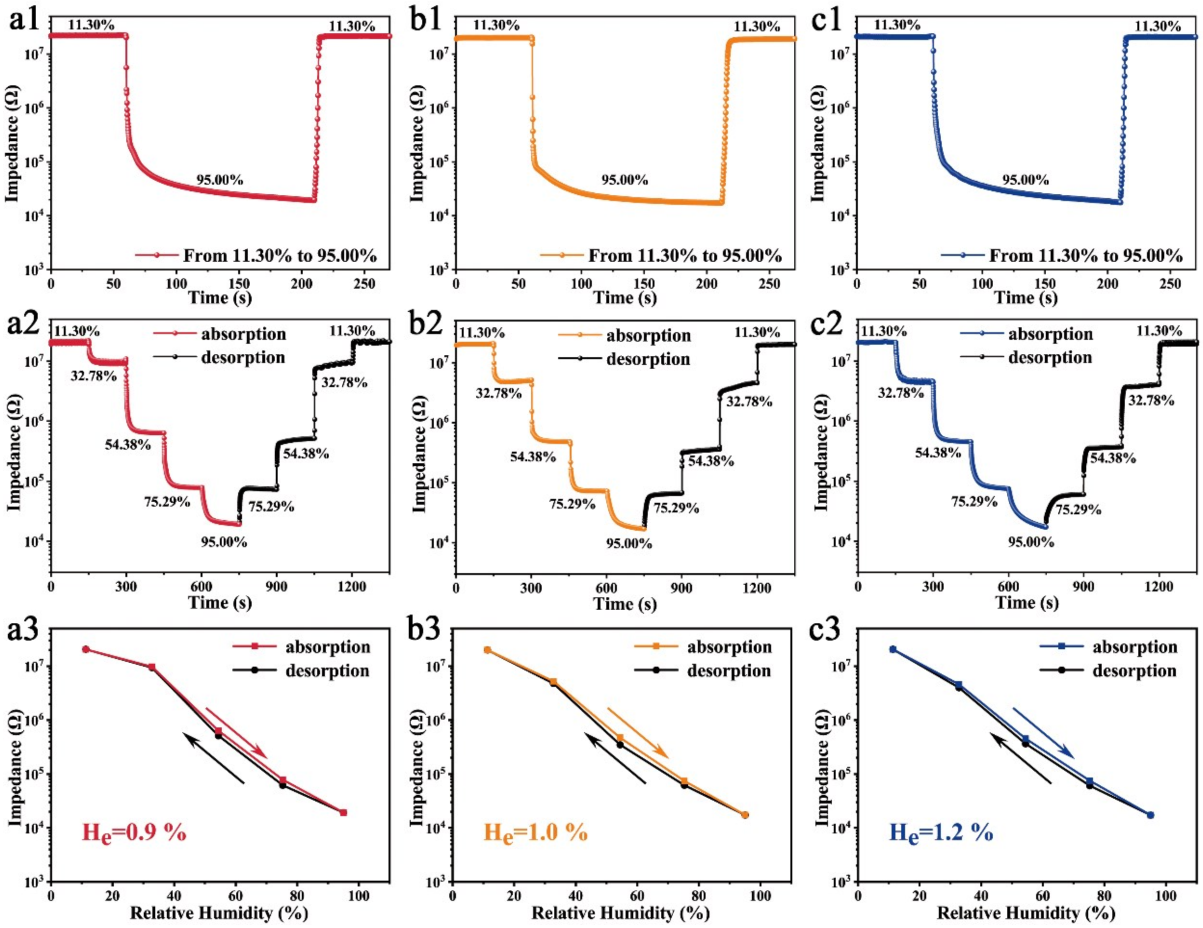

Fig. S22. (a1-c1) Response-recovery curves from 11.30% RH to 95.00% RH, (a2-c2) dynamic response-recovery characteristics from 11.30% RH to 95.00% RH, (a3-c3) humidity hysteresis of Ho_2O_3 nanosheets film sensor with thicknesses (a1-a3) 2 μm, (b1-b3) 3.2 μm, (c1-c3) 4.3 μm.

Take Ho_2O_3 nanosheet materials as an example. Prepared three humidity sensors with film thicknesses of 2 μm, 3.2 μm, and 4.3 μm, respectively, under the premise that the nanomaterial film can exist stably on the electrode surface (Fig. S21). It is found that the response time of the three sensors from 11.30% RH to 95.00% RH is still less than 300 ms, and the recovery time is still about 6 s. The sensitivity is 1137, 1143 and 1215, and the humidity hysteresis is 0.9%, 1.0% and 1.2%, respectively (Fig. S22). These results indicate that the change of film thickness has almost no effect on the response-recovery time of the material. The material sensitivity gradually increases as the film thickness increases, but the rate of change is small, which may be caused by the fact that the material has more surface to adsorb water molecules due to the change in the thickness of the material. The humidity hysteresis of the material also increases, which may be due to the fact that, there may be some effect on the desorption of water molecules as the thickness increases, but the effect is small. The thickness of the sample, however, has an effect on the sensitivity of the material in a low moisture environment, which decreases with decreasing thickness of the sample. Since the sensor tends to fall off from the surface of the forked finger electrode during calcination and testing when the hand-applied film is too thick. Finally choose the film material with a thickness of about 3.2 μm for testing.

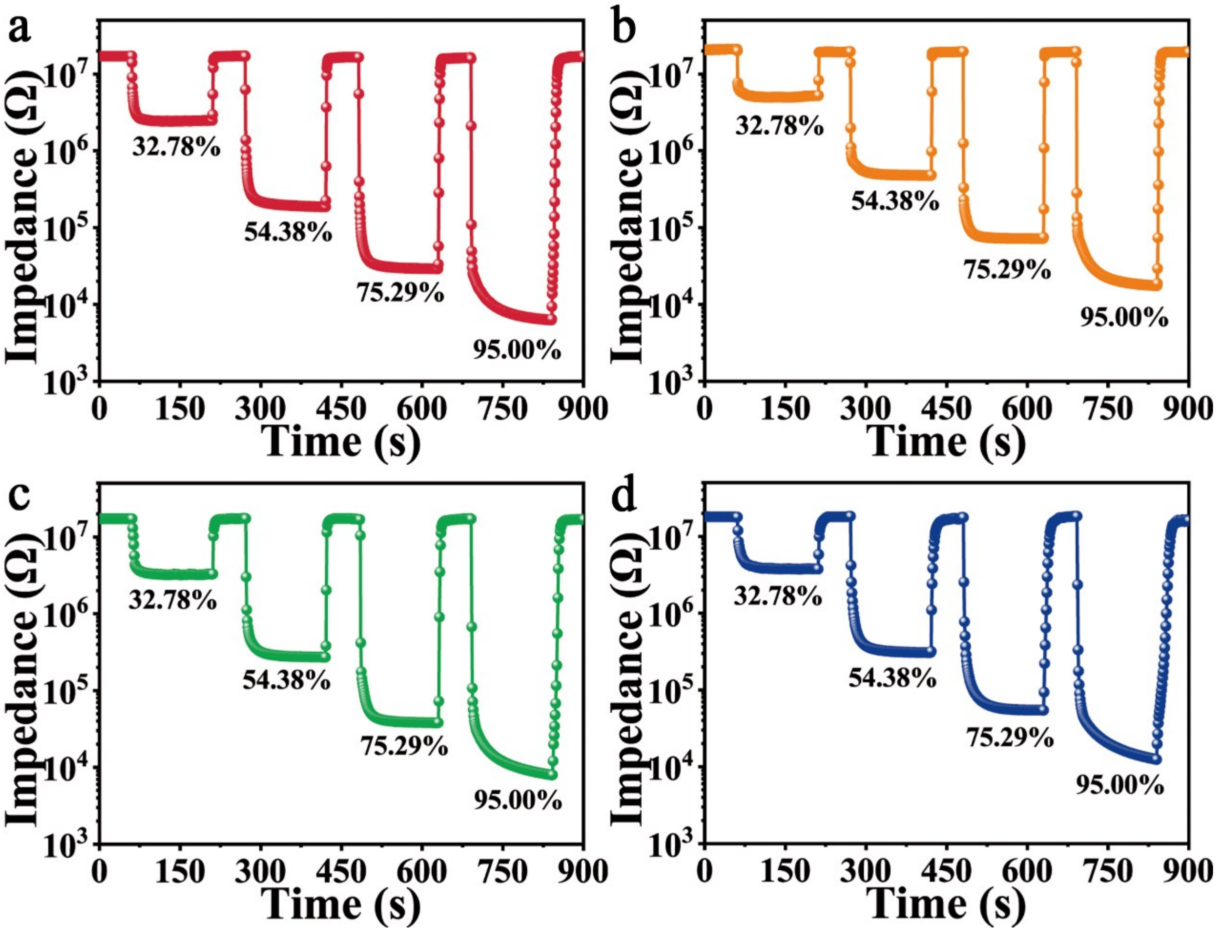

Fig. S23. Continuous response-recovery curves of four Ho_2O_3 materials of a) NT, b) NS, C) NTS, d) NSS from 11.30% RH to different environment humidity.

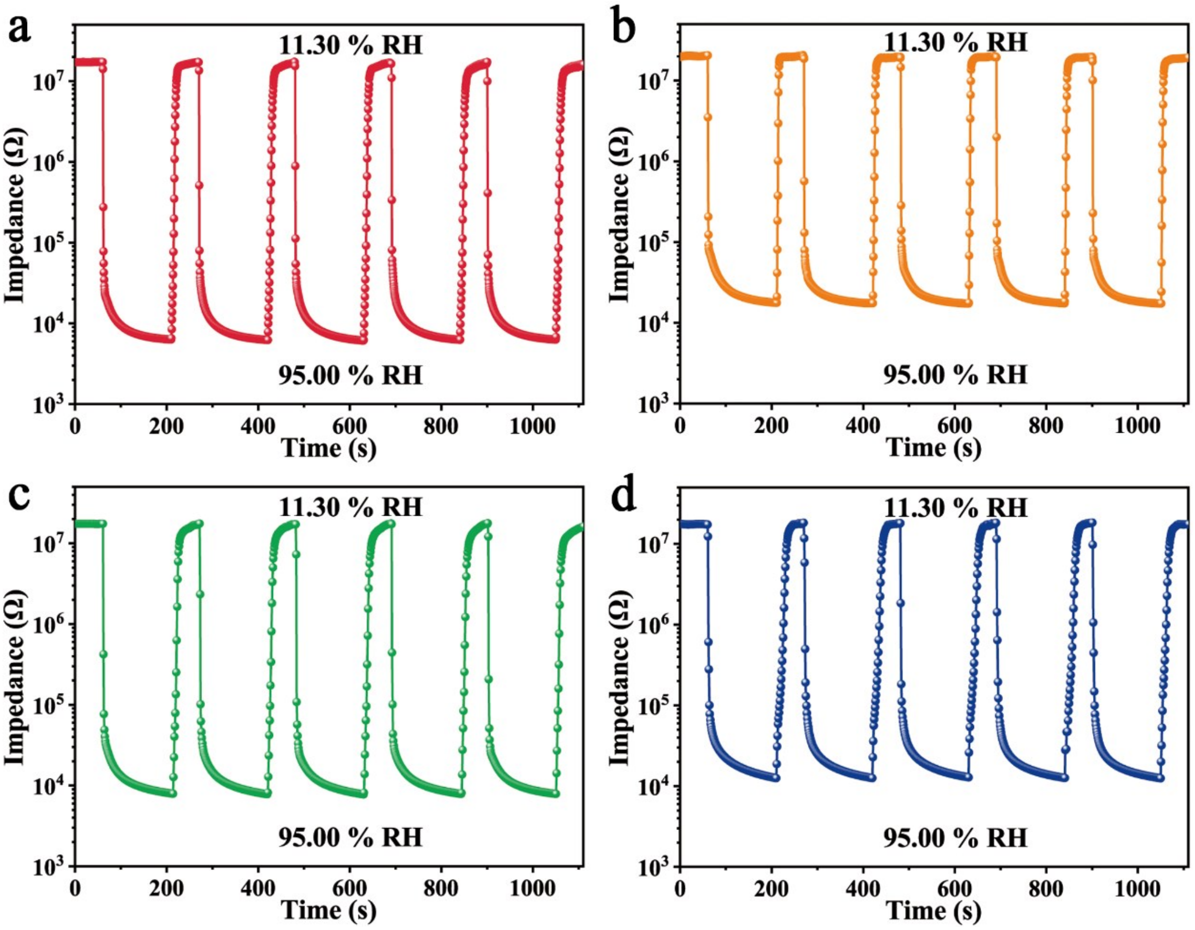

Fig. S24. Continuous response-recovery curves of four Ho_2O_3 materials of a) NT, b) NS, C) NTS, d) NSS from 11.30% RH to 95.00% RH environment.

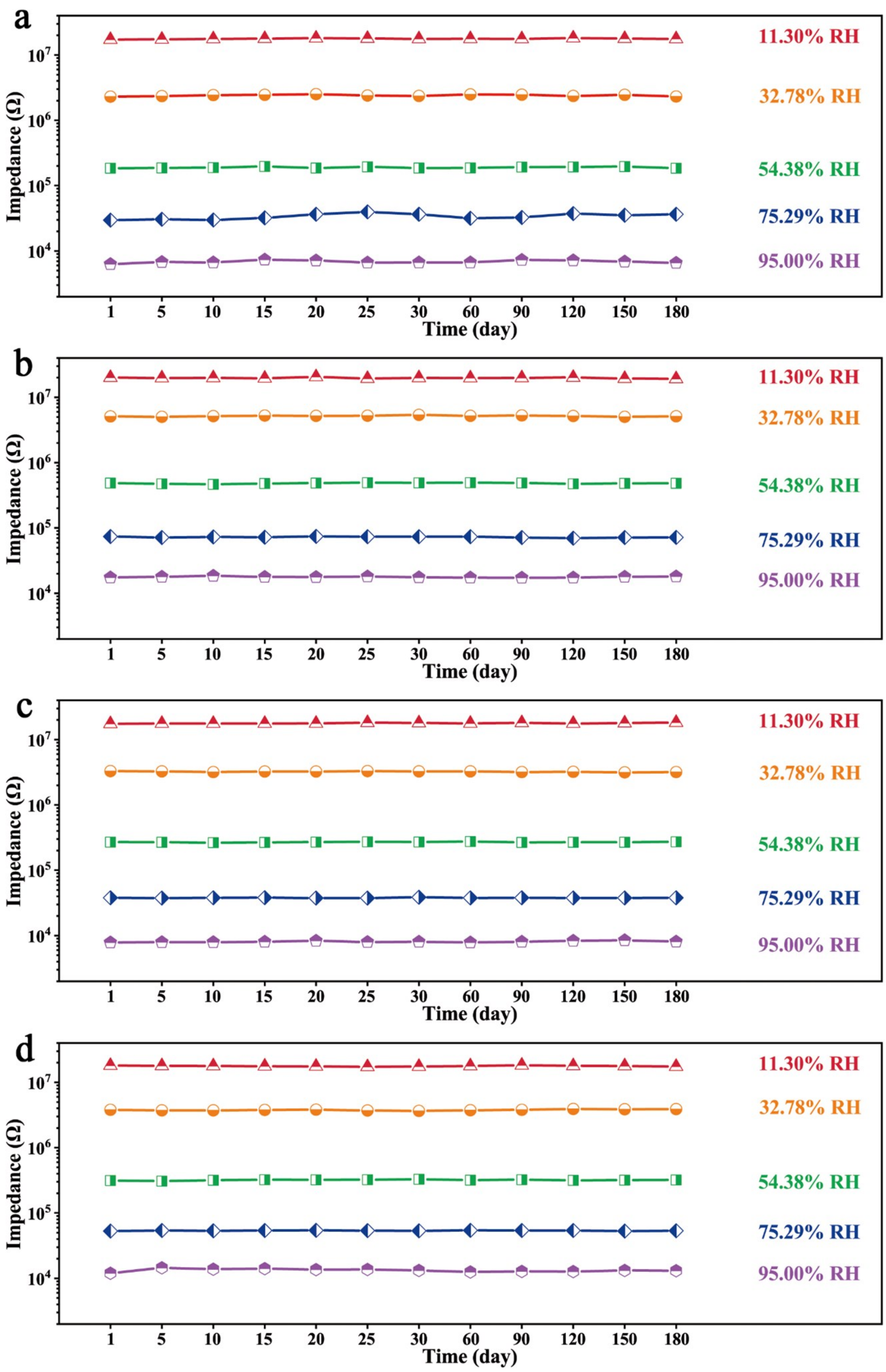

Fig. S25. Long-term stability of Ho_2O_3 a) NT, b) NS, c) NTS, d) NSS humidity sensor.

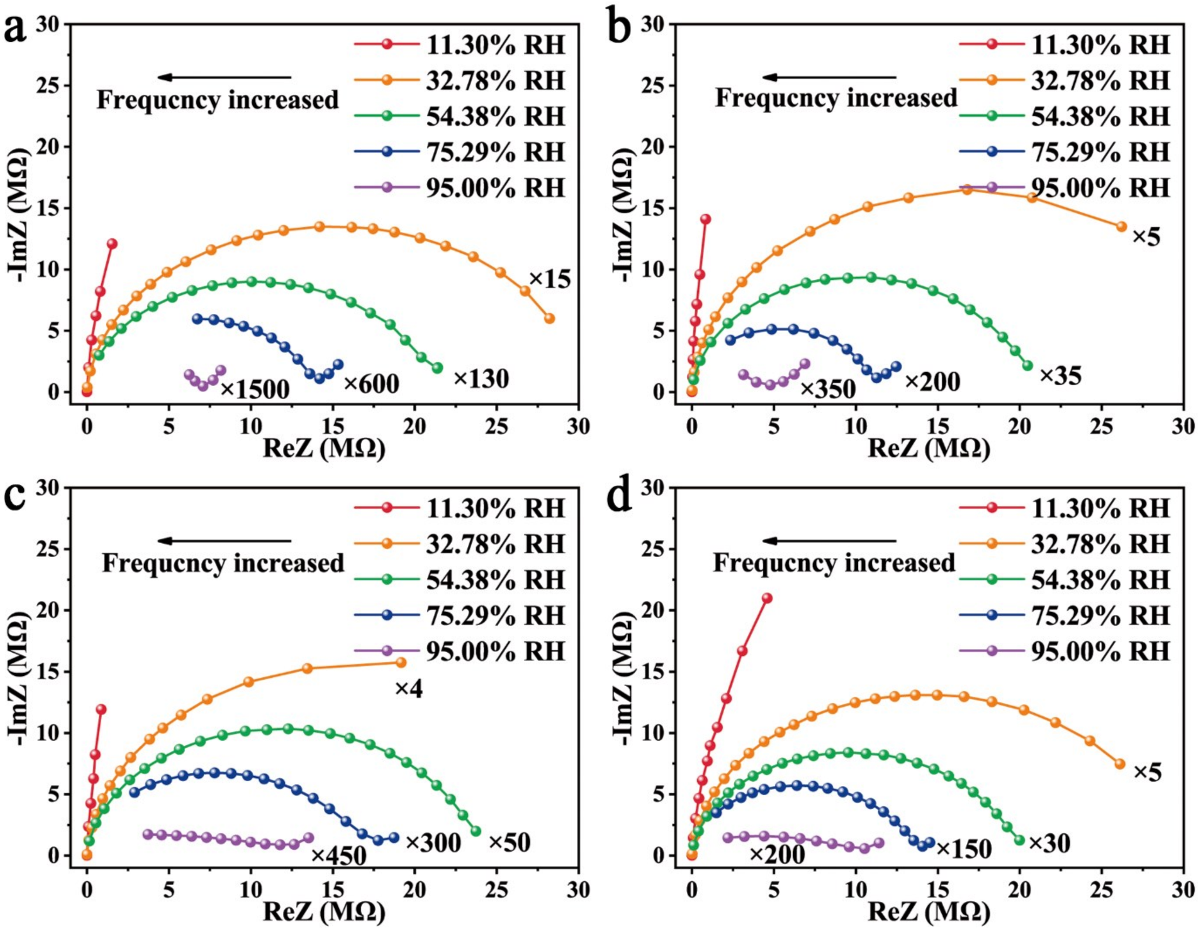

Fig. S26. Complex impedance spectra of Ho_2O_3 a) NT, b) NS, c) NTS, d) NSS humidity sensors at different humidity.

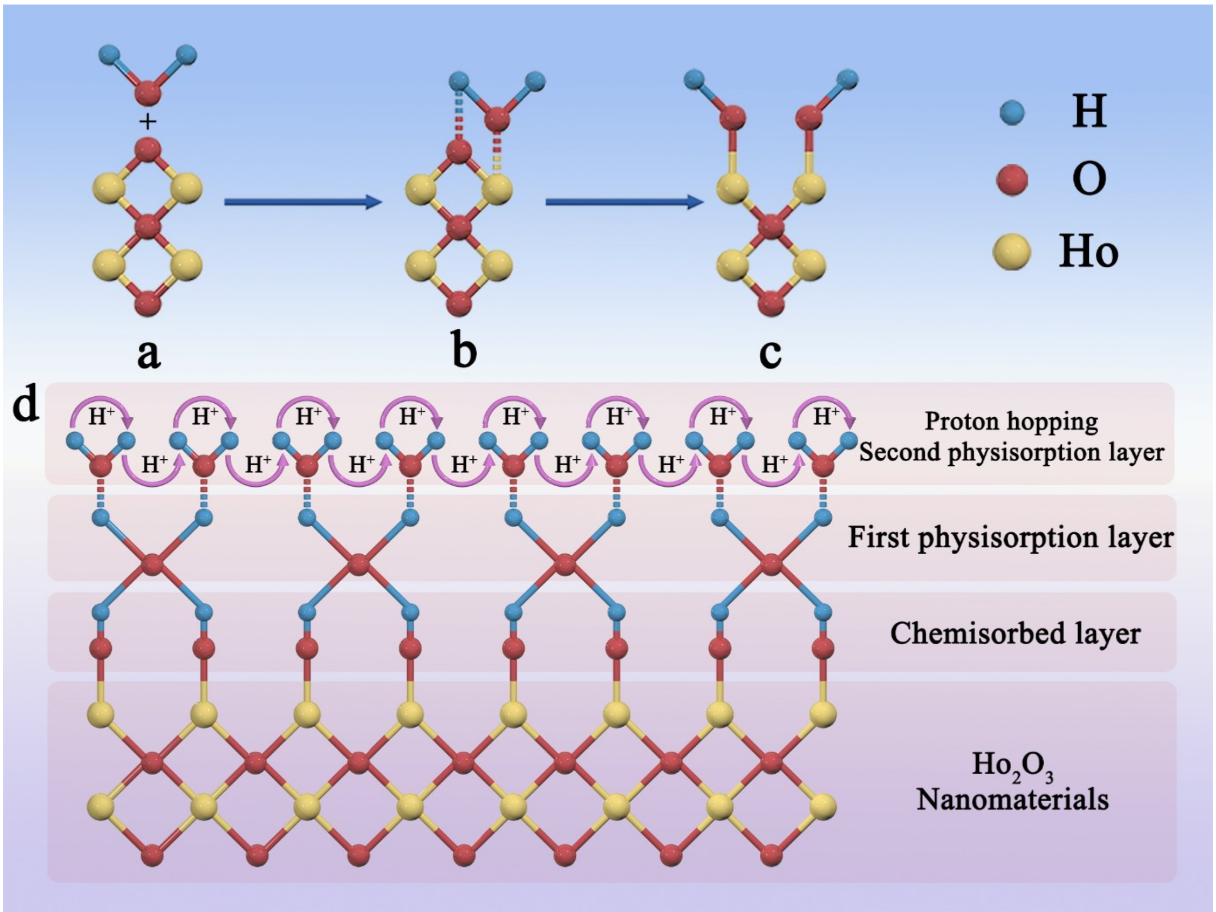

Fig. S27 Humidity sensitive mechanism of Ho_2O_3 nanomaterials.

In order to explain the sensing mechanism, complex impedance analysis was carried out (Fig. S26). Under the condition of 11.30% RH and low humidity, the complex impedance spectra show a semicircular part, at which time only a small amount of water molecules are adsorbed on the surface of Ho_2O_3 to form surface hydroxyl groups. As shown in Fig. S27 the water molecules are chemically adsorbed on the active sites on the oxide surface to form complex (Fig. S27b), subsequently, the complex is transferred to surface hydroxyl groups (Fig. S27c).[8] The Humidity Sensitive Mechanism shows in Fig. S27d. At this time, because the surface cannot form a continuous water molecular layer, the impedance value of the material is large, it is difficult for protons to migrate on the surface.[8] When the humidity is in the range of 32.78% RH - 54.38% RH, it can be seen in the complex impedance spectra that part of the semicircle becomes the whole semicircle at this humidity, due to the polarization of water molecules and the formation of polarized charge to participate in the conductivity. More water molecules are chemically adsorbed on the surface of the material to form more hydroxyl groups. At the same time, protons jump between hydroxyl groups for charge transfer.[8-10] When the humidity is in the range of 54.38% RH-95.00% RH, the water layer gradually thickens with the increase of humidity. As can be seen in the complex impedance spectra, a straight line is produced at the low frequency at this humidity, which is the stage of physical adsorption. At this stage, the H_2O molecule is decomposed into H_3O^+ and OH^-, Protons in H_3O^+ are transferred to the adjacent H_2O molecules by the action of electrostatic field, and the adjacent H_2O molecules become H_3O^+, then continue to transfer to the adjacent H_2O molecules and cycle infinitely, resulting in the Grottuss reaction: $H_2O+H_3O^+=H_3O^++H_2O$. At this time, protons transfer charge through ion transition.[7,11] The results show that all the Ho_2O_3 NT, NS, NTS, NSS show similar humidity sensing mechanism.

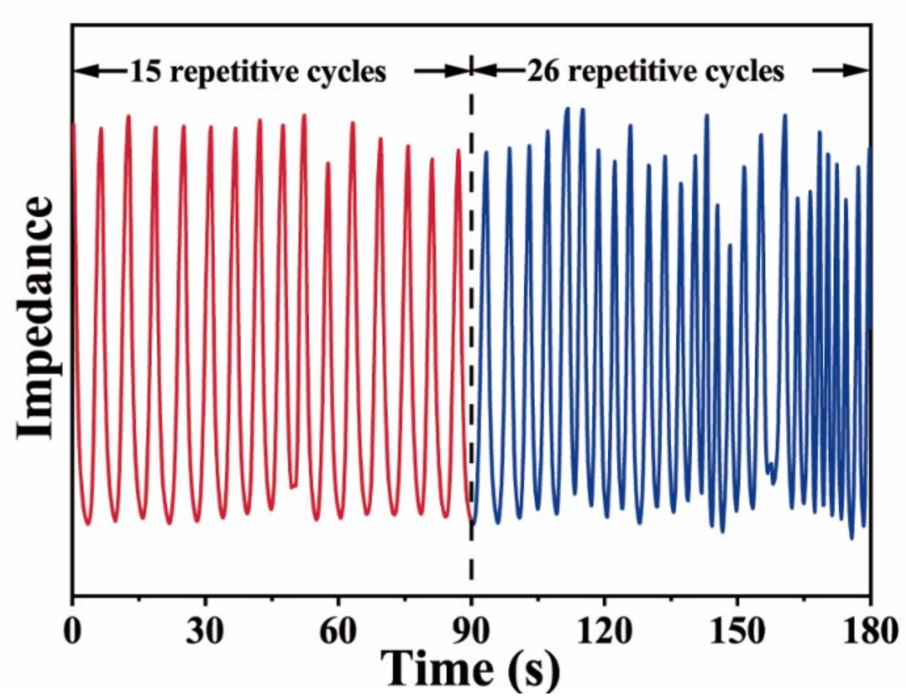

Fig. S28. Continuous breath monitoring in relaxing and sporting state.

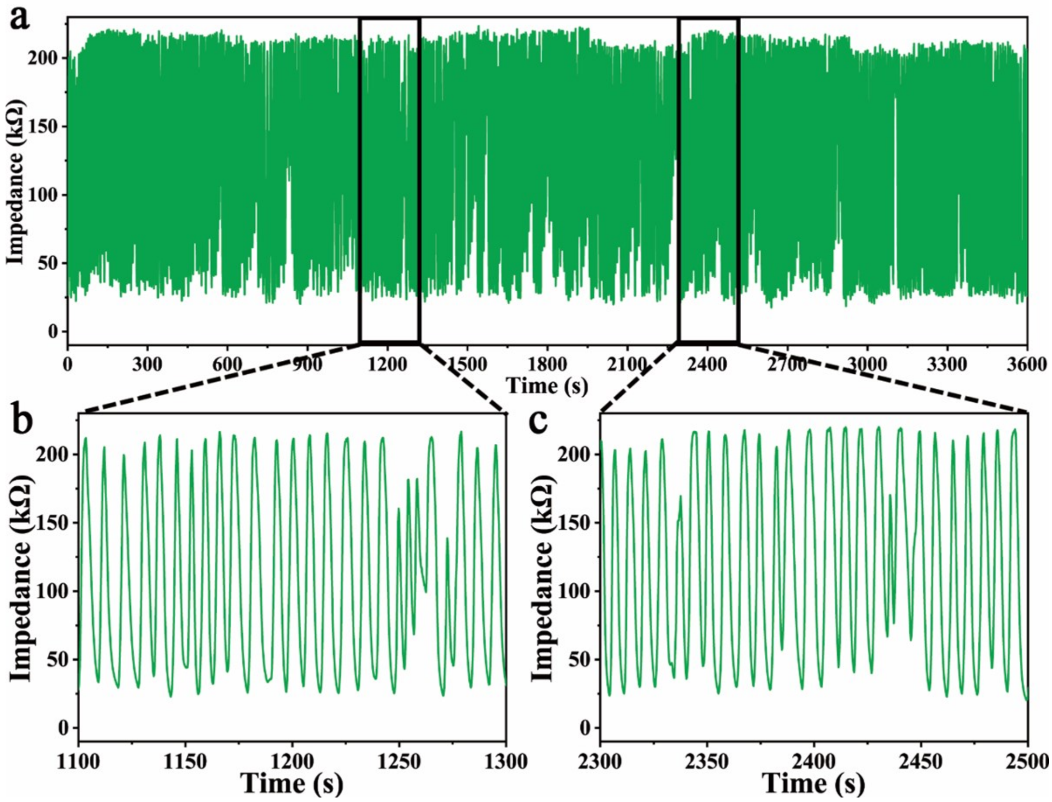

Fig. S29. (a) Long-term stability test chart of Ho_2O_3 NS sensor in simulated breath test. Enlarged image of (b) 1100-1300 s and (c) 2300-2500 s.

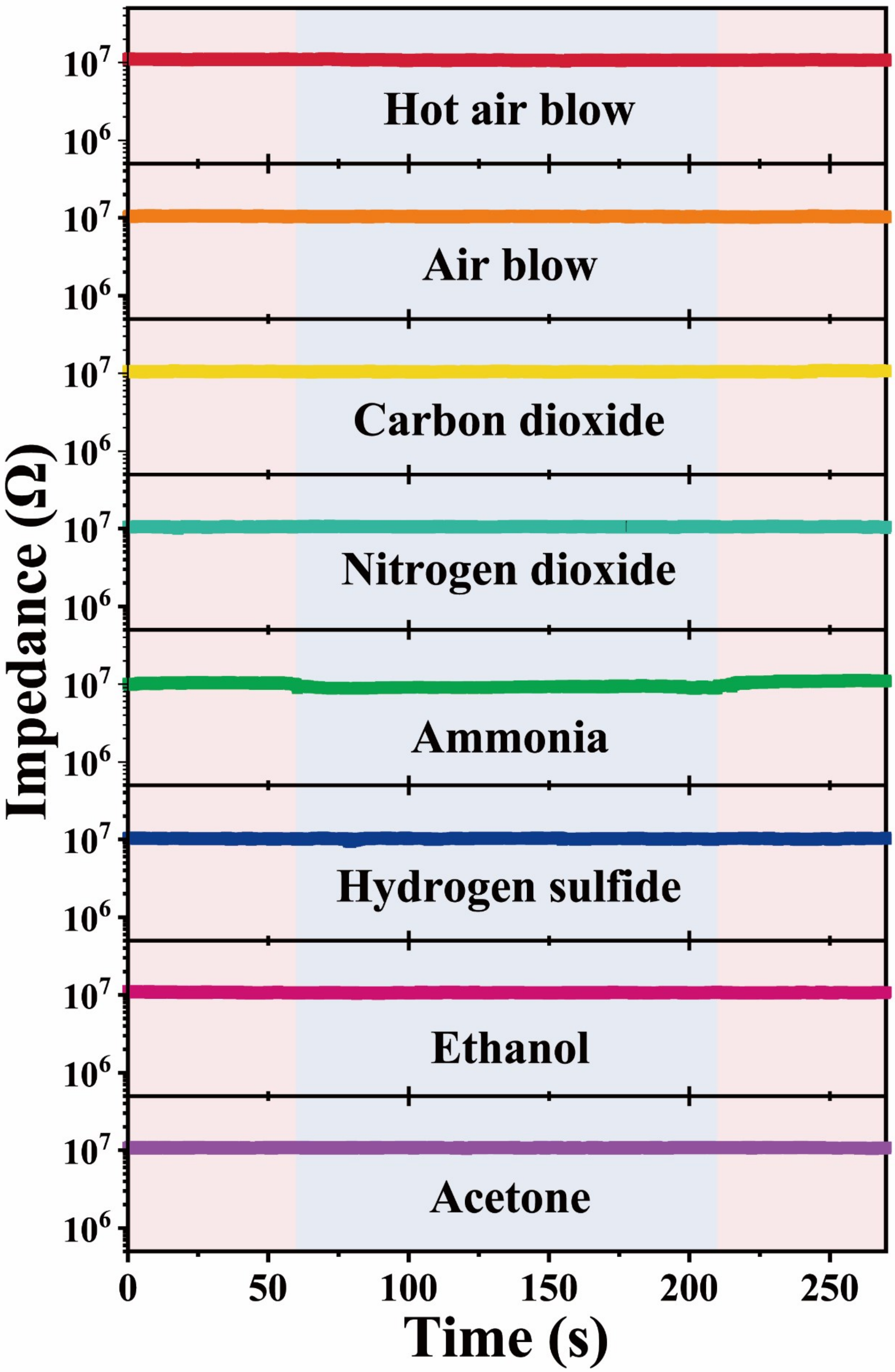

Fig. S30. The sensitivity curves of the sensor to air flow and different gases.

Fig. S30 shows the response-recovery curve of the sensor to 60℃ hot air, 25℃ airblow, 100 ppm CO_2, 10 ppm NO_2, 100 ppm NH_3, 100 ppm H_2S, 100 ppm ethanol, and 100 ppm acetone. The material was put into the test gas to be tested at 60 s and put back into the air atmosphere at 210 s. The test results show that the material only has a very small sensitivity of 1.18 in the 100 ppm NH_3, and does not respond to other several gases. Therefore, the material has good immunity to interference and can better produce accurate recognition of humidity changes as well as human breath.

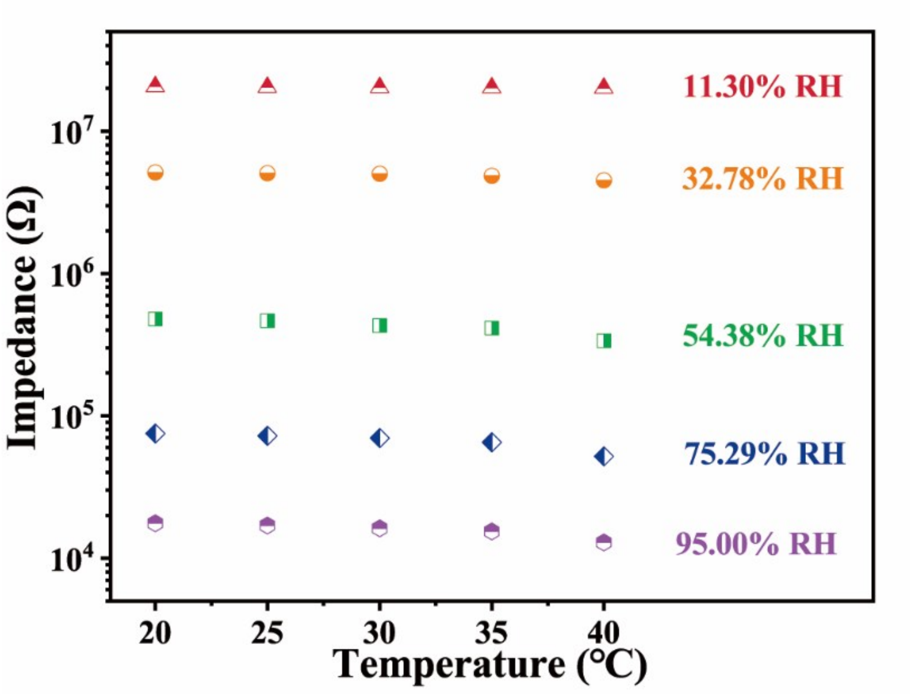

Fig. S31. Impedance of the sensor at different atmospheric temperatures.

Placed the sensing material in 20-40°C (common human exhaled gas temperature) for different operating environment temperature tests (Fig. S31). The results show that the impedance value of the material changes less in the low humidity environment. As the humidity gradually increases, the impedance value of the material gradually decreases and the effect gradually becomes obvious. Therefore, the sensor's operating environment temperature has less effect on the material in the temperature range of 20-40°C.

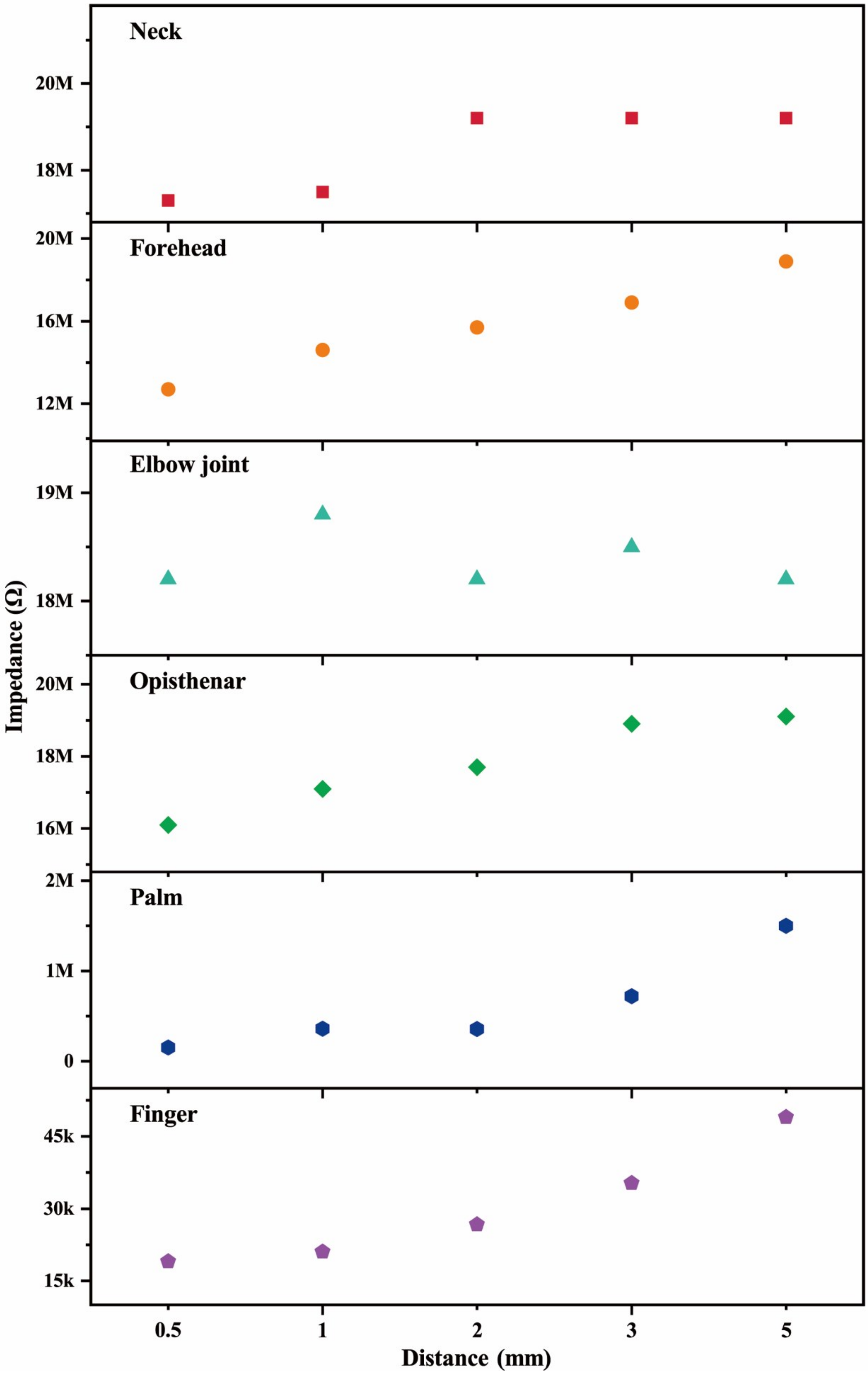

Fig. S32. Response values of the sensor to different test parts at different test distances.

We use human body surface with obvious humidity changes as the test sample for the typical test. When the sensor measures the human body surface humidity of the sweaty parts such as fingers and palms, the sensor can respond to the human body surface humidity when the test distance is 5 mm, and the impedance value of the sensor decreases gradually with the decrease of the test distance. However, when the sensor tests the parts that are not easy to sweat, such as neck and elbow, the sensor hardly produces a response if the test distance is greater than 1 mm. In order to ensure the high sensitivity of the test and the protection of the sensor surface and the safety of the test sample during the test, the best test distance between the sensor and test sample surface is set at 1 mm.

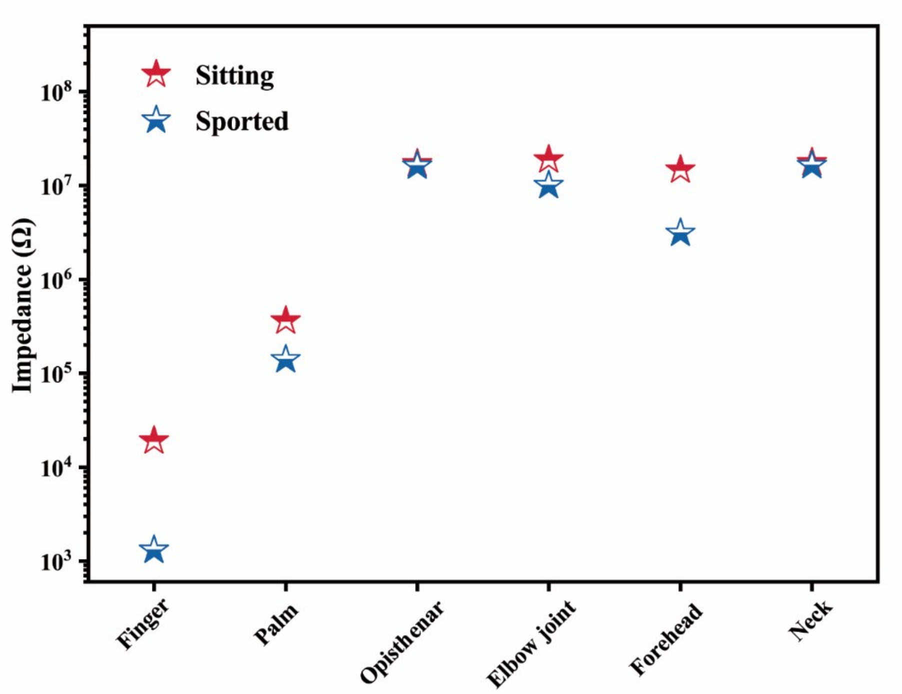

Fig. S33. The humidity of different parts of the same volunteer before and after exercise was tested.

References

[1] P. Lilli, P. Tlkka, H. Helena and P. Paavo, Thermochim. Acta 2003, **403**, 197-206.

[2] Z. Y. Xu, Y. J. Zhang, Z. Y. Fang, X. B. Yin and W. Zhu, Mater. Res. Bull. 2010, **45**, 74-79.

[3] S. K. Hussain, G. Nagaraju, E. Pavitra, G. S. R. Raju and J. S. Yu, CrystEngComm 2015, **17**, 9431-9442.

[4] Y. J. Zhang, K. D. Han, T. Cheng and Z. Y. Fang, Inorg. Chem. 2007, **46**, 4713-4717.

[5] S. Zinatloo-Ajabshir, S. Mortazavi-Derazkola and M. Salavati-Niasari, J. Mol. Liq. 2017, **231**, 306-313.

[6] N. Sakly, A. H. Said and H. Ben Ouada, J Mater Sci: Mater Electron 2015, **26**, 3440-3449.

[7] D. Z. Zhang, Y. E. Sun and Y. Zhang, ACS Appl. Mater. Interfaces 2016, **8**, 14142-14149.

[8] Y. Zhang, H. F. Zou, J. F. Peng, Z. H. Duan, M. Ma, X. Xin, W. L. Li and X. J. Zheng, Sens. Actuators, B 2018, **272**, 459-467.

[9] Z. Y. Li, H. N. Zhang, W. Zheng, W. Wang, H. M. Huang, C. Wang, A. G. MacDiarmid and Y. Wei, J. Am. Chem. Soc. 2008, **130**, 5036-5037.

[10] X. Zhao, X. D. Chen, X. Yu, P. Xu, N. Li and X. P. Chen, IEEE Sens. J. 2017, **17**, 6148-6152.

[11] J. Y. Zhang, Y. H. Zhen, H. Y. Xue, X. X. Gao, W. X. Wang, Y. D. Li, T. Hayat and N. S. Alharbi, Sens. Actuators, B 2019, **283**, 643-650.